

Revealing a main-sequence star that consumed a planet with JWST

RYAN M. LAU,¹ JACOB E. JENCSON,² COLETTE SALYK,³ KISHALAY DE,⁴ ORI D. FOX,⁵ MATTHEW J. HANKINS,⁶
MANSI M. KASLIWAL,⁷ CHARLES D. KEYES,⁵ MORGAN MACLEOD,⁸ MICHAEL E. RESSLER,⁹ AND SAM ROSE⁷

¹*NSF NOIRLab, 950 N. Cherry Ave., Tucson, AZ 85719, USA*

²*IPAC, Mail Code 100-22, Caltech, 1200 E. California Blvd. Pasadena, CA 91125*

³*Department of Physics and Astronomy, Vassar College, 124 Raymond Avenue, Poughkeepsie, NY 12604, USA*

⁴*MIT-Kavli Institute for Astrophysics and Space Research, 77 Massachusetts Ave., Cambridge, MA 02139, USA*

⁵*Space Telescope Science Institute, 3700 San Martin Drive, Baltimore, MD 21218, USA*

⁶*Arkansas Tech University, 215 West O Street, Russellville, AR 72801, USA*

⁷*Division of Physics, Mathematics, and Astronomy, California Institute of Technology, Pasadena, CA 91125, USA*

⁸*Center for Astrophysics — Harvard & Smithsonian 60 Garden Street, MS-16, Cambridge, MA, 02138, USA*

⁹*Jet Propulsion Laboratory, California Institute of Technology, MS 169-327, 4800 Oak Grove Drive, Pasadena, CA 91109*

Submitted to AAS Journals

ABSTRACT

The subluminous red nova (SLRN) ZTF SLRN-2020 is the most compelling direct detection of a planet being consumed by its host star, a scenario known as a planetary engulfment event. We present JWST spectroscopy of ZTF SLRN-2020 taken +830 d after its optical emission peak using the NIRSpec fixed-slit 3–5 μm high-resolution grating and the MIRI 5–12 μm low-resolution spectrometer. NIRSpec reveals the ^{12}CO fundamental band ($\nu = 1-0$) in emission at $\sim 4.7 \mu\text{m}$, Brackett- α emission, and the potential detection of PH_3 in emission at $\sim 4.3 \mu\text{m}$. The JWST spectra are consistent with the claim that ZTF SLRN-2020 arose from a planetary engulfment event. We utilize DUSTY to model the late-time $\sim 1\text{--}12 \mu\text{m}$ spectral energy distribution (SED) of ZTF SLRN-2020, where the best-fit parameters indicate the presence of warm, 720_{-50}^{+80} K, circumstellar dust with a total dust mass of $\text{Log}\left(\frac{M_d}{M_\odot}\right) = -10.61_{-0.16}^{+0.08} M_\odot$. We also fit a DUSTY model to archival photometry taken +320 d after peak that suggested the presence of a cooler, $T_d = 280_{-20}^{+450}$ K, and more massive, $\text{Log}\left(\frac{M_d}{M_\odot}\right) = -5.89_{-3.21}^{+0.29}$, circumstellar dust component. Assuming the cool component originates from the ZTF SLRN-2020 ejecta, we interpret the warm component as fallback from the ejecta. From the late-time SED model we measure a luminosity of $L_* = 0.29_{-0.06}^{+0.03} L_\odot$ for the remnant host star, which is consistent with a $\sim 0.7 M_\odot$ K-type star that should not yet have evolved off the main sequence. If ZTF SLRN-2020 was not triggered by stellar evolution, we suggest that the planetary engulfment was due to orbital decay from tidal interactions between the planet and the host star.

Keywords: Circumstellar matter — Stellar mergers — Planetary system evolution — Star-planet interactions

1. INTRODUCTION

The recent discovery of the subluminous red nova (SLRN) ZTF SLRN-2020 presented the most compelling detection of a planetary engulfment event, where a $\lesssim 10$ Jupiter-mass planet is believed to have been consumed

by its Sun-like host star (De et al. 2023; Soker 2023). Such events provide unique insight into the evolution of planetary systems, especially for the population of short-orbital-period ($\lesssim 10$ days) “hot Jupiters” (Dawson & Johnson 2018). In particular, engulfment events capture the end stage of a planet influenced by dynamical processes (e.g. Rasio & Ford 1996; Chatterjee et al. 2008) and/or the post-main sequence evolution of its host star (Xu et al. 2017; MacLeod et al. 2018a; Stephan

et al. 2020; Grunblatt et al. 2023; Yarza et al. 2023). Anomalous chemical signatures from stars have notably been associated with planetary engulfments due to the incorporation of planetary material in the outer layers of the star (Laughlin & Adams 1997; Pinsonneault et al. 2001; Spina et al. 2021; Soares-Furtado et al. 2021). The IR-luminous observational signatures of planetary engulfment events also probe the dusty and self-obscured physics of stellar coalescence, an important mechanism in the formation and evolution of stars. (De Marco & Izzard 2017; Kashi & Soker 2017; Kashi et al. 2019; Matsumoto & Metzger 2022; MacLeod et al. 2022; Wolf et al. 2024).

ZTF SLRN-2020 was initially identified as a nova-like, transient optical outburst by the Zwicky Transient Facility (ZTF; Bellm et al. 2019) and coincided with a luminous IR counterpart captured by the ongoing mid-IR survey from the Near-Earth Object Wide-field Infrared Survey Explorer (NEOWISE) Reactivation mission (Mainzer et al. 2014). Nova-like optical transients are notably common in the Galactic disk and typically attributed to dwarf novae, classical novae, or young stellar outbursts. However, a key characteristic of those scenarios are strong atomic emission lines indicative of hot gas, while spectroscopic observations of ZTF SLRN-2020 during its outburst revealed an almost featureless, red continuum (De et al. 2023). Molecular features from ZTF SLRN-2020 such as TiO, VO, and CO were later revealed by ground-based near-IR spectroscopic follow-up from instruments like TripleSpec on the 200-inch Hale Telescope at the Palomar Observatory (P200) and the Near-Infrared Echellette Spectrometer (NIREs) on the Keck-II Telescope (Wilson et al. 2004; Herter et al. 2008) that instead suggested the presence of a cool outer photosphere consistent with an M-type giant with a temperature of around 3600 K (De et al. 2023). These cool molecular features as well as the short-lived optical outburst and persistent IR emission exhibited by ZTF SLRN-2020 are hallmarks of an emerging class of transients known as “red novae,” which are associated with merger of two stars (Munari et al. 2002; Tylenda et al. 2011; Ivanova et al. 2013; Karambelkar et al. 2023).

A comparison of ZTF SLRN-2020’s low optical luminosity, $\sim 10^{35}$ erg s $^{-1}$, and $\lesssim 100$ d outburst duration, both of which are proportional to the companion mass, against the luminosity and duration of red novae from stellar-mass mergers demonstrated ZTF SLRN-2020 is consistent with the merger of a star and planet-mass companion (See Fig. 1 from De et al. 2023). Similar to the stellar-mass mergers, the optical outburst from ZTF SLRN-2020 was likely powered by hydrogen recombination in the ejected material while the IR-luminous

Table 1. Observations of ZTF SLRN-2020

Observatory	Obs. Date (MJD)	Wavelength	Obs. Mode
Gemini-N/NIRI	59809	J (1.25 μm), H (1.65 μm)	Imaging
JWST/NIRSpec	59827	3–5 μm	Fixed-Slit Spec. (R ~ 2700)
JWST/MIRI	59827	5–12 μm	Low-Resolution Spec. (R ~ 100)

NOTE—Summary of the $\sim 1 - 12$ μm observations of ZTF SLRN-2020 presented in this work from Gemini-N/NIRI, JWST/NIRSpec, and JWST/MIRI.

aftermath arises from the formation of circumstellar dust (MacLeod et al. 2022; De et al. 2023). Observations of the ZTF SLRN-2020 progenitor from the United Kingdom Infrared Telescope (UKIRT) Galactic Plane survey (Lawrence et al. 2007) provided constraints on the stellar component as a Sun-like, 0.8–1.5 M_{\odot} star assuming a distance of 4 kpc (De et al. 2023).

The mechanism triggering the planetary engulfment event in ZTF SLRN-2020 is, however, uncertain since the progenitor mass range is consistent with a star that is either on or evolving off the main sequence. It is therefore unclear whether dynamical processes such as tidal decay of the orbit and/or post-main sequence stellar evolution of the host star played the dominant role in the engulfment. The properties of circumstellar material from the ejecta of the planetary engulfment were also uncertain due to the lack of sensitive mid-IR follow-up capabilities at the time of the ZTF SLRN-2020 outburst. JWST’s sensitive mid-IR spectroscopic capabilities are therefore ideal to probe the dusty aftermath of ZTF SLRN-2020 and investigate the open questions on planetary engulfment events.

In this paper, we present late-time (+830 d) 3–12 μm spectroscopic follow-up observations with JWST and near-contemporaneous ground-based near-IR photometry from Gemini-North. The JWST and Gemini-N observations are described in Sec. 2. In Sec. 3, we identify notable features from the ZTF SLRN-2020 observations and investigate the properties of the circumstellar material. We also re-analyze earlier (+320 d) ZTF SLRN-2020 photometry from De et al. (2023) using DUSTY to investigate the evolving circumstellar dust properties. We then discuss the implications of the circumstellar and remnant host star properties and address the nature of ZTF SLRN-2020 in Sec. 4.

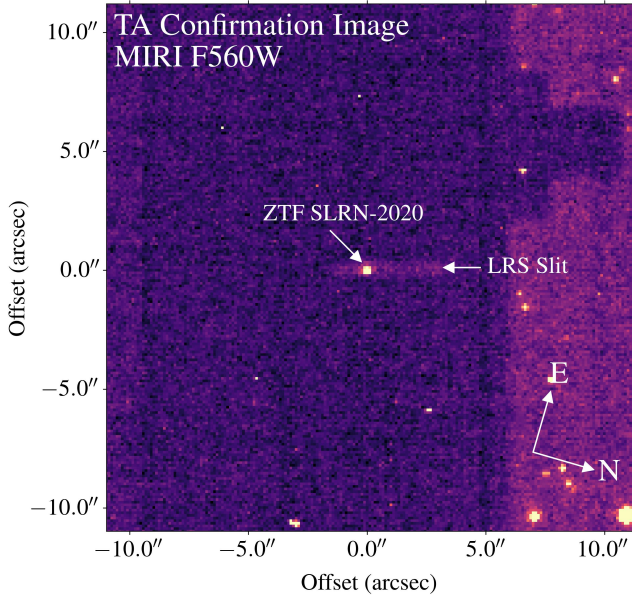


Figure 1. JWST/MIRI target acquisition (TA) confirmation image for the LRS observations of ZTF SLRN-2020 taken on 2022 September 5 with the F560W filter. ZTF SLRN-2020 is shown within the $4.7 \times 0.51''$ LRS slit.

2. OBSERVATIONS AND DATA REDUCTION

2.1. JWST/NIRSpec Fixed Slit Spectroscopy

ZTF SLRN-2020 was observed with JWST on 2022 September 5 in Cycle 1 as part of the program GTO 1240 (PI M. Ressler). ZTF SLRN-2020 was one of three targets of opportunity observed in GTO 1240 and was selected based on the detection of its IR-luminous counterpart from NEOWISE (De et al. 2023). Spectroscopic observations of ZTF SLRN-2020 covering $\sim 3 - 12 \mu\text{m}$ were obtained using NIRSpec Fixed Slit Spectroscopy and MIRI Low Resolution Spectroscopy in a non-interruptible sequence.

NIRSpec observations utilized the $3.2 \times 0.2''$ S200A1 slit with the G395H/F290LP Grating/Filter combination to cover a wavelength range of $\lambda = 2.9 - 5.1 \mu\text{m}$ with a resolving power of ~ 2700 . Note that the physical gap in the NIRSpec detectors results in a wavelength gap between 3.69 and $3.79 \mu\text{m}$ for the fixed-slit G395H/F290LP observations. Target acquisition (TA) was performed on the same target as the science observation (i.e. ZTF SLRN-2020) using the NIRSpec Wide Aperture TA (WATA) method with the SUB2048 subarray, F140X filter, and the NRSRAPID acquisition readout pattern. The target acquisition image was inspected to ensure that ZTF SLRN-2020 was successfully acquired, which was important given its location in a crowded field with close nearby sources (De et al. 2023).

Observations of ZTF SLRN-2020 with NIRSpec were performed using the NRSIRS2RAPID readout pattern with the FULL subarray and two primary dither positions with no sub-pixel dithers. The total exposure time was 13.6 min with 28 groups per integration and two integrations (one per dither position). The NIRSpec observations were reduced using version 1.16.0 of the JWST science calibration pipeline with the 1298 CRDS context. The raw `uncal` files were downloaded from the Mikulski Archive for Space Telescopes (MAST)¹ and run through each stage of the pipeline. The accuracy of the wavelength calibration for the high resolution ($R \sim 2700$) grating is $\sim 15 \text{ km s}^{-1}$, or $\sim 1/8$ of a resolution element (Böker et al. 2023).

The `extract_1d` step was re-run on the reduced level 3 NIRSpec `s2d` file using a $0.8''$ aperture with `ystart` = 19 and `ystop` = 26. Since the observations were taken with two primary dither positions, no additional background subtraction was utilized in the `extract_1d` step. For the DUSTY spectral energy distribution analysis (Sec. 3.3), the spectrum was smoothed by convolving with a Gaussian kernel with a full width at half maximum (FWHM) of 12 pixels. Figure 2 presents the convolved and non-convolved NIRSpec spectra of ZTF SLRN-2020 as well as spectra that have been dereddened to correct for the estimated interstellar extinction ($A_V \approx 3.6 \text{ mag}$; De et al. 2023). A 2% spectrophotometric uncertainty is adopted across the NIRSpec spectrum (Böker et al. 2023). The root-mean-square noise of the observed spectrum over the spectral pixels in the apparently featureless $3.0 - 4.0 \mu\text{m}$ wavelength range is $5.5 \mu\text{Jy}$.

2.2. JWST/MIRI Low Resolution Spectroscopy

JWST/MIRI observations of ZTF SLRN-2020 with the low-resolution spectrometer (LRS) covered $5 - 12 \mu\text{m}$ with a resolving power of $R \sim 100$ and were obtained on 2022 September 5 in a non-interruptible sequence with the NIRSpec observations. Due to the uncertain $5.6 \mu\text{m}$ emission from ZTF SLRN-2020 prior to the JWST observations, a nearby bright star was used for an offset target acquisition. The F560W TA confirmation image shown in Fig. 1 was taken to verify ZTF SLRN-2020 was successfully aligned in the $4.7 \times 0.51''$ LRS slit. The MIRI LRS observations of ZTF SLRN-2020 were taken with the FULL subarray using the FASTR1 readout pattern and the 2-pt ALONG SLIT NOD dither type. The total MIRI LRS exposure time on ZTF SLRN-2020 was 13 min with 140 groups per integration/dither.

¹ <https://mast.stsci.edu/portal/Mashup/Clients/Mast/Portal.html>

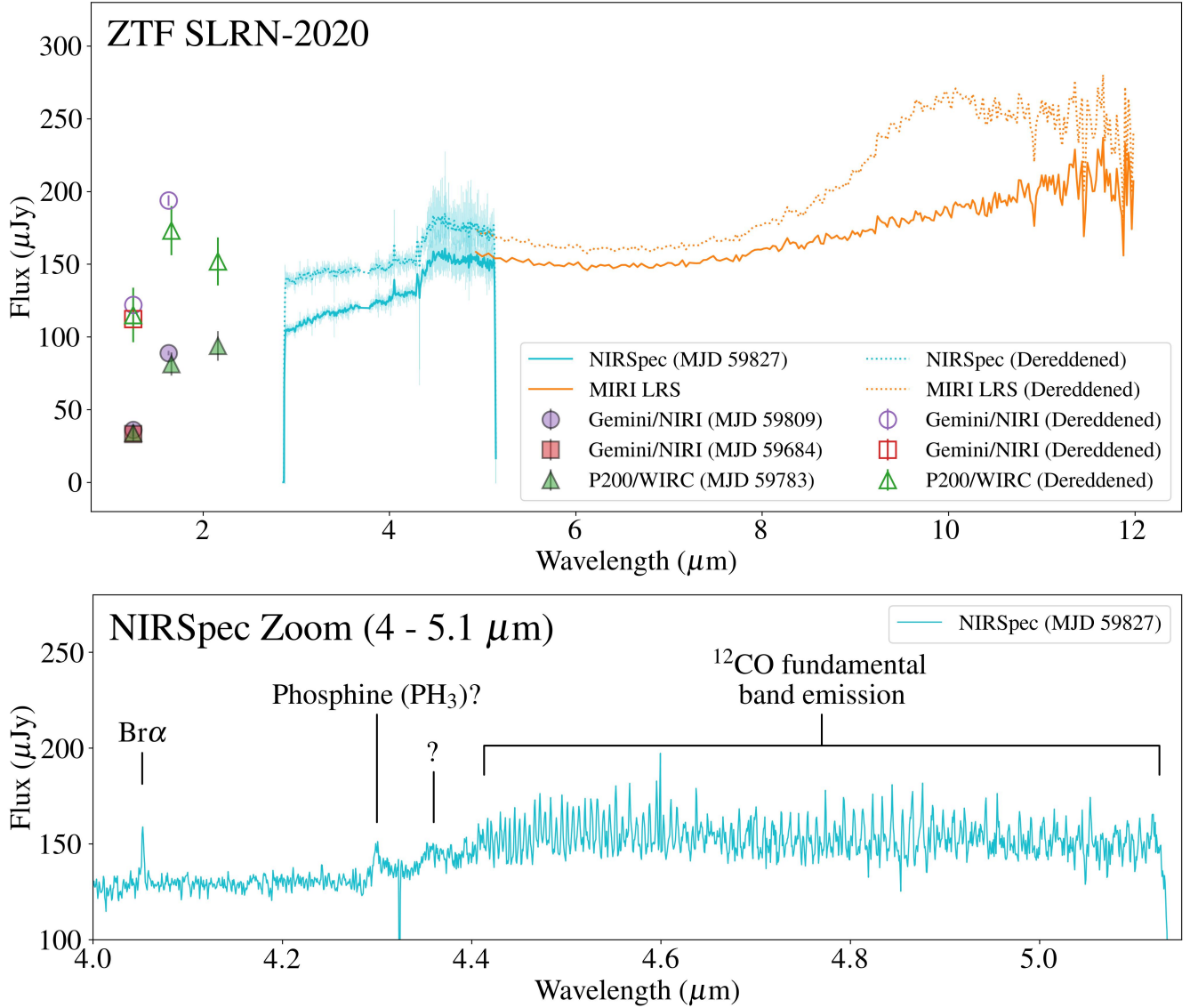


Figure 2. (Top) Observed and dereddened+normalized spectral energy distribution of ZTF SLRN-2020 taken by Gemini/NIRI, P200/WIRC, JWST/NIRSpec, and JWST/MIRI LRS. NIRSpec and MIRI observations were taken on the same day (MJD 59827) in a non-interruptible sequence. The NIRSpec spectrum has been smoothed by convolving with a Gaussian with a 12-pixel FWHM and is overlaid on the non-convolved spectrum. Note that an additive normalization has been applied to the NIRSpec spectrum as described in Sec. 2.3. (Bottom) Observed NIRSpec spectrum overlaid with notable spectroscopic features. The apparent narrow absorption “feature” to the right of the potential PH_3 feature is likely an artifact due to a bad pixel.

The MIRI LRS data were reduced with version 1.16.0 of the JWST science calibration pipeline with the 1298 CRDS context. The default output from the `extract_1d` step from the pipeline was used for the analysis in this work. The 4.9–12 μm range of the LRS spectrum is shown in Fig. 2 both before and after dereddening to correct for interstellar extinction. A 5% spectrophotometric uncertainty is adopted across the LRS spectrum (Wright et al. 2023).

2.3. NIRSpec-MIRI Normalization

In the overlapping 4.9–5.1 μm wavelength range between the NIRSpec and MIRI spectra there is a 6.0 μJy (4%) offset in the flux density. Figure 2 shows this offset, where the MIRI spectrum is slightly brighter than the NIRSpec spectrum in the 4.9–5.1 μm wavelength range. In order to normalize the NIRSpec and MIRI spectra for spectral analysis and spectral energy distribution (SED) fitting, a negative offset of 6.0 μJy was applied to the entire MIRI spectrum. The normalization was applied to the MIRI spectrum since the 4% difference from the overlapping NIRSpec range falls within

the 5% spectrophotometric uncertainty (Wright et al. 2023). This normalized MIRI spectrum is used for the data analysis.

2.4. Ground-based Near-IR Imaging

We obtained high spatial resolution Adaptive Optics (AO) assisted imaging using the Near-Infrared Imager (NIRI) on the Gemini North telescope (Hodapp et al. 2003). The source was observed on UT 2022-08-18 as part of a Director’s Discretionary Program (GN-2022A-DD-106; PI: K. De). We obtained dithered exposures of the field using Laser Guide Star (LGS) correction for a total exposure time of 60 s, 60 s and 120 s in J , H and K bands respectively. The raw images were detrended and stacked using the DRAGONS pipeline (Labrie et al. 2019), using the source catalog from NIR images of the field presented in De et al. (2023) for astrometric and photometric calibration. We measured J and H (Vega) magnitudes of $J = 19.08 \pm 0.04$ and $H = 17.66 \pm 0.02$, but we were unable to obtain a photometric solution for the K -band observations due to clouds.

3. RESULTS AND ANALYSIS

3.1. Late-Time Infrared Emission from ZTF SLRN-2020

The late-time, ground-based and JWST observations of ZTF SLRN-2020 obtained $\gtrsim 750$ d after its i -band peak (MJD 58993; De et al. 2023) are shown in Figure 2 and reveal a “red” continuum rising from ~ 30 to $\sim 200 \mu\text{Jy}$ between $\sim 1 - 12 \mu\text{m}$. Near-IR photometry from Gemini-N taken on 2022 August 18 (MJD 59809) is notably consistent with P200 ($J = 19.17 \pm 0.15$, $H = 17.75 \pm 0.09$, and $Ks = 17.13 \pm 0.10$ mag) and previous Gemini-N ($J = 19.17 \pm 0.05$ mag) observations reported by De et al. (2023) that were taken on 2022 July 23 (MJD 59783) and 2022 April 15 (MJD 59684), respectively. The stability in the near-IR over the 4-month timescale suggests it probes emission from the photosphere of the remnant star as opposed to cooling circumstellar dust. The mid-IR $\gtrsim 4 \mu\text{m}$ emission that increases towards longer wavelengths likely traces thermal continuum emission from circumstellar dust.

The dereddened IR emission from ZTF SLRN-2020 was corrected for interstellar extinction using the $R(V) = 3.1$ model from the `dust_extinction v1.3.2` python package (Gordon et al. 2023) adopting a foreground extinction of $A_V = 3.6$ mag (De et al. 2023). Although the dereddened spectral energy distribution (SED) exhibits the $9.7 \mu\text{m}$ silicate emission feature, its

Table 2. ZTF SLRN-2020 Br α Emission Line Properties

Parameter	Value
Amplitude	$(6.30 \pm 0.49) \times 10^{-19} \text{ erg s}^{-1} \text{ cm}^{-2} \text{ \AA}^{-1}$
Peak Position	$4.0526 \pm 0.0001 \mu\text{m}$
FWHM	$0.0016 \pm 0.0001 \mu\text{m}$
Line Flux	$(2.5 \pm 0.4) \times 10^{-17} \text{ erg s}^{-1} \text{ cm}^{-2}$

NOTE—Derived Br α emission line properties from the best-fit Gaussian model.

presence is speculative because it appears only after dereddening the apparently featureless mid-IR continuum observed by the LRS. The shape and strength of the feature in the dereddened spectrum is therefore determined by the adopted A_V and the profile of the silicate emissivity in the Gordon et al. (2023) extinction correction.

The SED of ZTF SLRN-2020 exhibits the following notable features:

- Emission peak in the near-IR at H -band ($1.64 \mu\text{m}$)
- Detection of Br α ($\lambda = 4.05 \mu\text{m}$) emission
- Potential detection of phosphine (PH $_3$) emission at $\sim 4.3 \mu\text{m}$
- ^{12}CO fundamental band ($\nu = 1 - 0$) emission at $\sim 4.7 \mu\text{m}$

Since thermal dust emission should not peak at such short wavelengths ($\lambda \sim 1.5 \mu\text{m}$) due to the ~ 1000 K sublimation temperature of dust grains, the presence of the near-IR peak in the dereddened spectrum supports the hypothesis that the near-IR emission traces the photosphere of the remnant star. The effective temperature and luminosity of the remnant star are investigated in more detail using DUSTY radiative transfer models in Sec. 3.3.

The NIRSpec spectrum reveals a $\sim 10\sigma$ detection of the Br α hydrogen recombination line from ZTF SLRN-2020. Previous optical and near-IR spectra of ZTF SLRN-2020 during its outburst presented by De et al. (2023) notably did not capture any atomic lines in emission. Utilizing the `specutils` Python package, we fit a Gaussian profile to the Br α line from the dereddened and continuum-subtracted NIRSpec spectrum (Fig. 3). The properties of the best-fit Br α emission line model are shown in Table 2. The detection of Br α suggests the presence of hot circumstellar gas, perhaps accreting onto the remnant star.

² <https://dust-extinction.readthedocs.io/en/stable/>

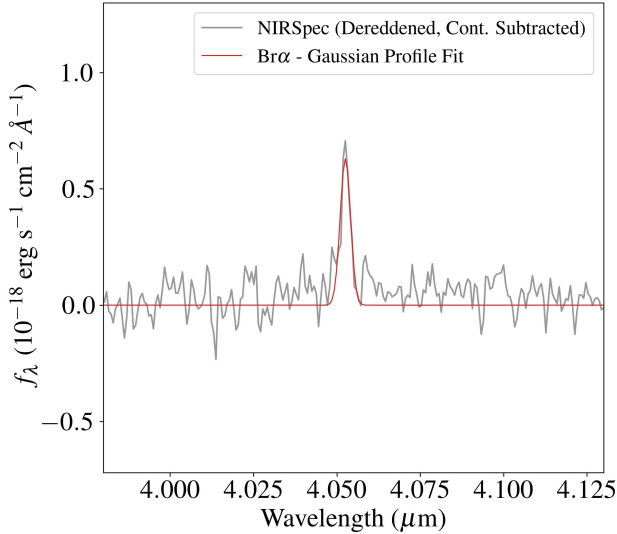


Figure 3. Best-fit Gaussian profile model of the Br α emission line detected from ZTF SLRN-2020 overlaid on the dereddened and continuum-subtracted JWST/NIRSpec spectrum.

A broad emission feature at $\sim 4.3 \mu\text{m}$ is present in the NIRSpec spectrum which we suggest is associated with the strongest emission band of phosphine (PH_3 ; See Sousa-Silva et al. 2020). PH_3 has previously been detected in the atmospheres of the gas giant planets Jupiter and Saturn (Bregman et al. 1975; Larson et al. 1977) as well as the circumstellar environment of the carbon-rich asymptotic giant branch (AGB) star IRC +10216 (Agúndez et al. 2014). Recent observations with JWST have also indicated the presence of PH_3 in the atmosphere of a brown dwarf based on the absorption signature of PH_3 between $4.0 - 4.4 \mu\text{m}$ (Burgasser et al. 2024). The second strongest PH_3 feature is a broad band between $8 - 11 \mu\text{m}$ (Sousa-Silva et al. 2020) is not present in the MIRI LRS spectrum of ZTF SLRN-2020. However, that PH_3 feature would be difficult to detect since the $8 - 11 \mu\text{m}$ wavelength range is dominated by thermal dust emission (See Sec. 3.3.1). Analysis of the suggested PH_3 feature from ZTF SLRN-2020 is presented in Sec. 3.5. Another broad emission feature appears at $\sim 4.35 \mu\text{m}$ that is unlikely related to PH_3 . The identification of the $\sim 4.35 \mu\text{m}$ feature is uncertain, but the feature may be blended with ^{12}CO fundamental band emission. The apparent narrow absorption “feature” between the 4.3 and $4.35 \mu\text{m}$ features is likely an artifact due to a bad pixel.

Utilizing `spectools_ir`, a suite of tools designed for analysis of molecular astronomical IR spectra, we confirm that the series of emission features around $\sim 4.7 \mu\text{m}$ in the NIRSpec spectrum of ZTF SLRN-2020 origi-

nates from ^{12}CO fundamental band emission. A model of the ^{12}CO fundamental band emission lines from `spectools_ir` is overlaid on the $4.4 - 5.1 \mu\text{m}$ spectrum of ZTF SLRN-2020 in Figure 4. Further analysis and details on the CO modeling is discussed in Sec. 3.2. The ^{12}CO fundamental band emission supports also supports presence of hot gas.

3.2. ^{12}CO Emission Modeling

We investigated the physical properties of circumstellar gas probed by the ^{12}CO fundamental band emission of ZTF SLRN-2020 utilizing the “slab” fitting tools `slabspec` and `slab_fitter` in `spectools_ir`³. The distance to ZTF SLRN-2020 was assumed to be $d = 4 \text{ kpc}$ (De et al. 2023). The `flux_calculator` tool in `spectools_ir` was used to compute CO line fluxes assuming Gaussian line profiles. The `slab_fitter` tool then uses the Markov Chain Monte Carlo (MCMC) fitting code `emcee` (Foreman-Mackey et al. 2013) to fit a slab model to the CO line fluxes measured from `flux_calculator`.

Based on the `slab_fitter` model to the CO emission features, we were able to derive the column density of emitting gas, N_{CO} , radius of the emitting region assuming a circular geometry, R_{C} , and the excitation temperature, T_{CO} . We then used `slabspec` to generate the ^{12}CO emission model spectrum in Figure 4 that was convolved with a $\Delta v = 120 \text{ km s}^{-1}$ FWHM Gaussian to match the approximate resolution of the NIRSpec spectrum. The model calculations and NIRSpec-detected lines of the ^{12}CO R- and P-branch transitions from ZTF SLRN-2020 are shown in the rotation diagram in Figure 5. The ^{12}CO emission model spectrum shows a close agreement with the observed features in the $4.4 - 5.1 \mu\text{m}$ wavelength range. Apparent emission features that are not reproduced by the model (e.g. See Fig. 4 between the R2 and R3 transitions) may be due to instrumental artifacts but warrant further investigation in a future study.

The best-fit `slab_fitter` model to the ^{12}CO emission from ZTF SLRN-2020 provided an excitation temperature of $T_{\text{CO}} = 1340^{+130}_{-110} \text{ K}$ with an emitting area of $\text{Log}(\frac{\Omega_{\text{CO}}}{\text{sr}}) = -19.64^{+0.11}_{-0.12}$ (or $9.8^{+2.8}_{-2.4} \times 10^{-10} \text{ arcsec}^2$) and a column density of $\text{Log}(\frac{N_{\text{CO}}}{\text{cm}^{-2}}) = 18.02^{+0.21}_{-0.16}$. Assuming a circular disk geometry for the emitting region of ^{12}CO , the disk radius is $R_{\text{CO}} = 15.2^{+2.0}_{-2.0} R_{\odot}$. The total ^{12}CO mass, M_{CO} , from such a disk can then be estimated as $N_{\text{CO}} \times \pi R_{\text{CO}}^2 \times m_{\text{CO}}$, where $m_{\text{CO}} (=$

³ This package is available on The Python Package Index (<https://pypi.org/project/spectools-ir/>) and version 1.0.0 is archived on Zenodo (Salyk 2022).

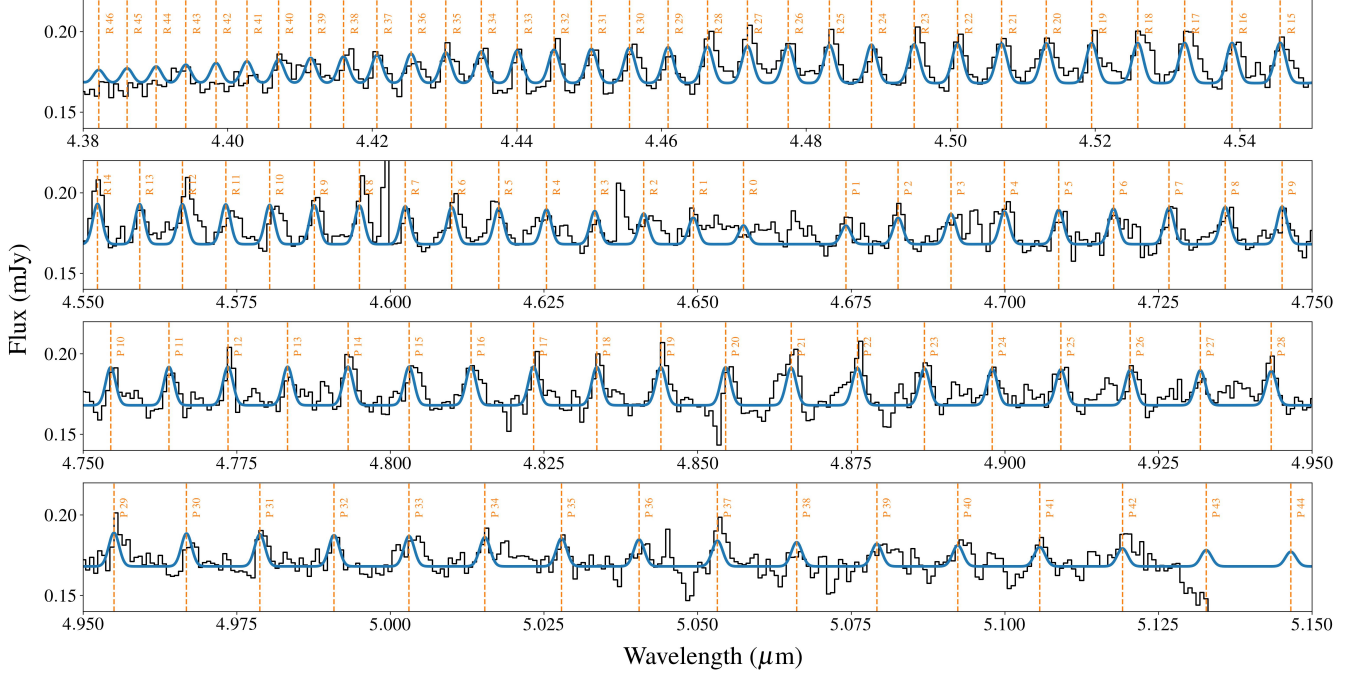


Figure 4. Dereddened NIRSpec G395H/F290LP spectrum of the ^{12}CO fundamental band emission between $4.38 - 5.15 \mu\text{m}$ from ZTF SLRN-2020 overlaid with the ^{12}CO model spectrum from `spectools_ir` and the wavelengths of the “R”- and “P”-branch transitions.

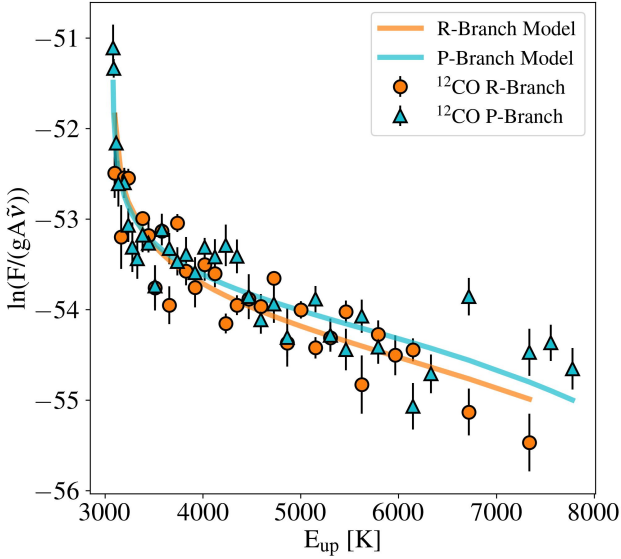


Figure 5. Rotation diagram (in CGS units) of the measured ^{12}CO R- and P-branch transitions from the NIRSpec spectrum of ZTF SLRN-2020 and the model output from `spectools_ir`. F is the integrated line flux and E_{up} is the upper level energy of the transition.

$4.65128 \times 10^{-23} \text{ g}$) is the mass of a ^{12}CO molecule. We therefore estimate

$$\text{Log} \left(\frac{M_{\text{CO}}}{M_{\odot}} \right) \approx -13.1^{+0.3}_{-0.3}, \quad (1)$$

Assuming that the gas traced by the ^{12}CO emission is fully molecular, approximately exhibits a solar abundance, and that the mass is dominated by molecular hydrogen H_2 , the total gas mass can be estimated as $M_{\text{CO}} \times N(\text{H}_2/^{12}\text{CO}) \times m_{\text{H}_2}/m_{\text{CO}}$, where $N(\text{H}_2/^{12}\text{CO})$ is assumed to be 10^4 and $m_{\text{H}_2}/m_{\text{CO}}$ is ≈ 0.071 . We estimate a total gas mass of

$$\text{Log} \left(\frac{M_{\text{gas}}}{M_{\odot}} \right) \approx -10.2^{+0.3}_{-0.3}. \quad (2)$$

Detection of the ^{12}CO fundamental band ($\nu = 1 - 0$) in emission is typically seen from embedded young stellar objects (YSOs; Pontoppidan et al. 2003; Herczeg et al. 2011), disks around Herbig Ae/Be stars (Blake & Boogert 2004), and T Tauri disks (Salyk et al. 2011). However, ^{12}CO fundamental band emission has notably been detected around V432 Sgr (Banerjee et al. 2004), a red nova that has been compared to ZTF SLRN-2020 given its low luminosity (De et al. 2023).

ZTF SLRN-2020 is unlikely associated with a YSO outburst or Herbig Ae/Be star due to the lack of atomic emission lines in the optical and near-IR spectrum taken during outburst (De et al. 2023). The CO excitation temperature we measure for ZTF SLRN-2020 is also much hotter than that observed from T Tauri disks (Salyk et al. 2011). The JWST spectra also do not exhibit any prominent ice absorption features, which are common for embedded YSOs. Addition-

Table 3. Model Results Summary

Parameter	Value
spectools_ir Best-fit ^{12}CO Model (+830 d, JWST)	
T_{CO}	1340^{+130}_{-110} K
$\text{Log}\left(\frac{\Omega_{\text{CO}}}{\text{sr}}\right)$	$-19.64^{+0.11}_{-0.12}$
R_{CO}	$15.2^{+2.0}_{-2.0}$ R_{\odot}
$\text{Log}\left(\frac{N_{\text{CO}}}{\text{cm}^{-2}}\right)$	$18.02^{+0.21}_{-0.16}$
$\text{Log}\left(\frac{M_{\text{CO}}}{M_{\odot}}\right)$	$-13.1^{+0.3}_{-0.3}$
$\text{Log}\left(\frac{M_{\text{gas}}}{M_{\odot}}\right)$	$-10.2^{+0.3}_{-0.3}$
DUSTY Best-fit SED Model (+830 d, JWST + P200)	
L_{*}	$0.29^{+0.03}_{-0.06}$ L_{\odot}
T_{d}	720^{+80}_{-50} K
τ_{V}	$0.7^{+0.3}_{-0.1}$
T_{*}	3500 K
R_{in}	$50.5^{+9.5}_{-11.0}$ R_{\odot}
$\text{Log}(M_{\text{d}})$	$-10.61^{+0.08}_{-0.16}$ M_{\odot}
DUSTY Best-fit SED Model (+320 d, ZTF + P200 + NEOWISE)	
L_{*}	$13.06^{+5.61}_{-10.76}$ L_{\odot}
T_{d}	280^{+450}_{-20} K
τ_{V}	$4.2^{+0.4}_{-3.6}$
T_{*}	5800^{+800}_{-2800} K
R_{in}	4730^{+1600}_{-4420} R_{\odot}
$\text{Log}\left(\frac{M_{\text{d}}}{M_{\odot}}\right)$	$-5.89^{+0.29}_{-3.21}$

NOTE—Best-fit model parameters from IR observations of ZTF SLRN-2020. The **spectools_ir** results were fit to the ^{12}CO fundamental band emission revealed by the JWST/NIRSpec spectrum taken +830 d from the emission peak. **DUSTY** SED models were fit to the dereddened, +830 d observations from NIRSpec, MIRI, and P200/WIRC. **DUSTY** SED models were also fit to dereddened archival +320 d observations taken by P48+ZTF, P200/WIRC, and NEOWISE +320 d from the emission peak. The interstellar extinction and distance of ZTF SLRN-2020 were assumed to be $A_{\text{V}} = 3.6$ and $d = 4$ kpc, respectively (De et al. 2023).

ally, the lack of polycyclic aromatic hydrocarbon (PAH) features between 6–12 μm in the LRS spectrum of ZTF SLRN-2020 likely rules out a Herbig Ae/Be origin given that they commonly exhibit PAH features (Keller et al. 2008). The JWST spectroscopic observations are therefore consistent with the claim that ZTF SLRN-2020 arose from a planetary engulfment event.

3.3. Circumstellar Dust Emission Modeling

3.3.1. SED Modeling of +830 d Epoch

In order to constrain the luminosity and effective temperature of the remnant star and investigate the circumstellar dust around ZTF SLRN-2020, we used the **DUSTY** radiative transfer code (Nenkova et al. 2000) to model its full 1–12 μm SED. We fit **DUSTY** SED models to the dereddened data that includes the P200/WIRC JHK_s photometry, smoothed NIRSpec 3–5 μm spectra with the ~ 4.7 μm ^{12}CO fundamental band emission removed, and the 5–12 μm LRS spectrum. Note that the ^{12}CO emission was removed from the fitting since **DUSTY** only models the emission from the heating source, scattered light, and thermal emission from circumstellar dust.

Using the **SPHERE** geometry, the input parameters related to the circumstellar dust were the dust composition, grain size distribution, sublimation temperature (T_{Sub}), dust temperature at the inner boundary (T_{d}), the shell thickness factor (Y)⁴, the dust density power-law of the shell (α), and the optical depth τ_{V} . The central radiative dust-heating source is assumed to be a blackbody with an effective temperature T_{*} , which is a free input parameter for the modeling. **DUSTY** outputs an SED model that includes the attenuated and non-attenuated heating-source spectrum, dust-scattered light, and thermal dust emission. **DUSTY** also calculates an inner dust shell radius (R_{in}) that assumes a fixed heating-source luminosity of $10^4 L_{\odot}$ with an effective temperature T_{*} . The output SED must then be normalized to the 1–12 μm SED of the ZTF SLRN-2020 to derive the heating-source luminosity and the inner shell radius. We therefore fit a multiplicative factor to scale the output SED to the ZTF SLRN-2020 SED. Adopting a distance of $d = 4$ kpc, the total stellar luminosity L_{*} can then be derived by integrating over the non-attenuated heating source spectrum scaled to the data. We utilized a reduced- χ^2 analysis to characterize the goodness-of-fit of the **DUSTY** SED model to the ZTF SLRN-2020 SED.

A standard Mathis et al. (1977) (MRN) distribution was adopted for the grain sizes that assumes minimum and maximum grain sizes of 0.005 μm and 0.25 μm , respectively, and a grain-size power-law index of -3.5 . Given the uncertainties in the grain composition, a 50/50 silicate/amorphous-carbon composition was adopted using the **Sil-0w** and **amC-Hn** optical properties provided by **DUSTY** (Ossenkopf et al. 1992; Hanner 1988). The dust sublimation temperature was fixed at value of $T_{\text{Sub}} = 1500$ K. Lastly, a $\propto r^{-2}$ radial dust-density profile and a shell thickness factor of $Y = 5$

⁴ i.e. the outer radius of the dust shell is $R_{\text{in}} \times Y$

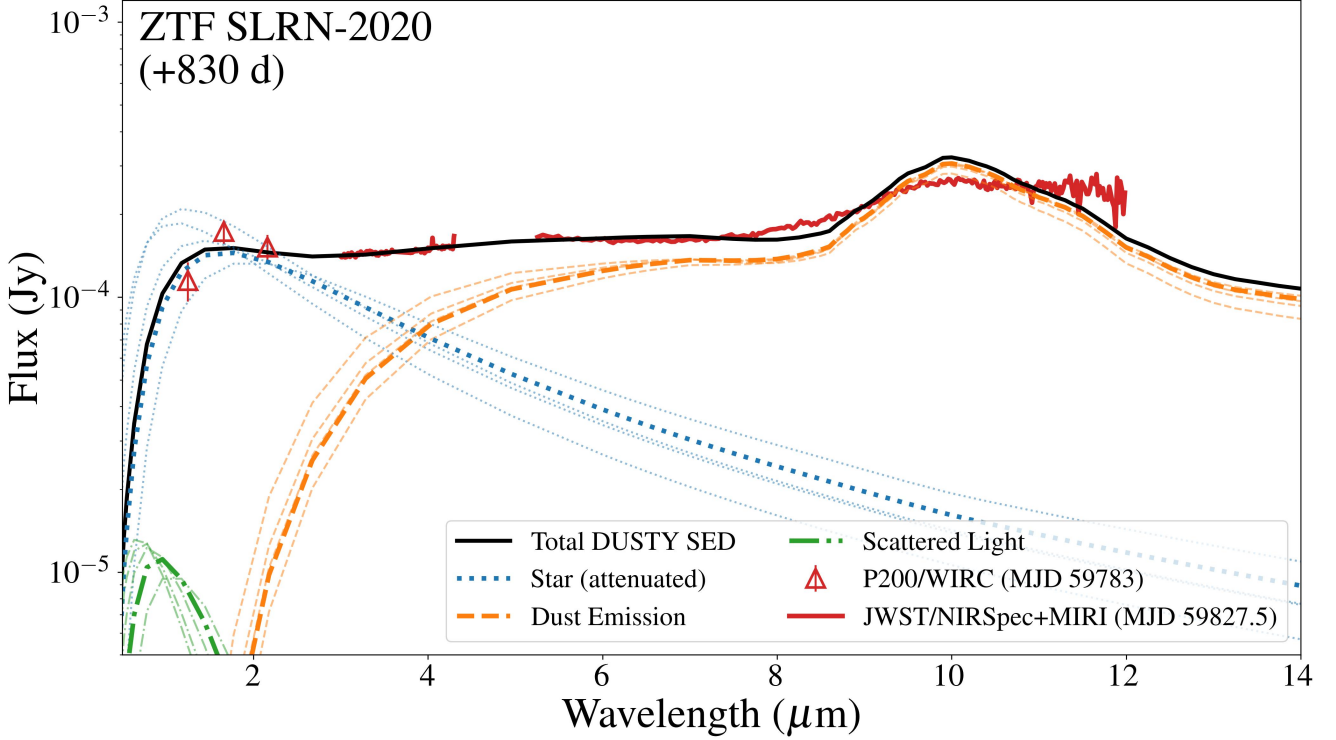


Figure 6. Best-fit DUSTY models of the ZTF SLRN-2020 SED from JWST and P200/WIRC data (+830 d epoch) using five different effective temperatures for the heating source (i.e. remnant star): $T_* = 3000, 3500, 4000, 4500$, and 5000 K. The $T_* = 3500$ K model (bold lines) provided the best fit to the P200/WIRC near-IR photometry. The solid black line shows the total $T_* = 3500$ K DUSTY SED model composed of the attenuated stellar emission (blue, dotted), dust emission (orange, dashed), and dust-scattered starlight (green, dot-dashed).

was adopted for the spherically symmetric circumstellar dust.

We note that the DUSTY SED analysis conducted by De et al. (2023) on ZTF SLRN-2020 also adopted the same grain size distribution, radial density profile, and shell thickness, but with a pure silicate dust composition. A pure silicate dust composition was attempted in our modeling but led to unsatisfactory fitting results. We emphasize the uncertainty on the grain composition given that the shape of the $9.7 \mu\text{m}$ silicate feature largely influenced from the interstellar extinction correction (Fig. 2)

We performed the SED-fitting by conducting a grid search across the inner boundary dust temperature T_d and the optical depth of the circumstellar dust shell τ_V . The values for T_d ranged from 500–1500 K with a step size of 25 K. The values for τ_V ranged from 0.1–5.0 with a step size of 0.1. Due to the limited coverage of the near-IR photometry probing direct emission from the heating source, the effective temperature of the heating source T_* is difficult to constrain with DUSTY models. We therefore performed the T_d - τ_V grid search described above using five different effective temperatures for the heating source (i.e. remnant star): $T_* = 3000,$

3500, 4000, 4500, and 5000 K. The results of the best-fit DUSTY SEDs for all five effective temperatures are shown in Figure 6, where the $T_* = 3500$ K model exhibited the best fit to the P200/WIRC near-IR photometry. We therefore favor the best-fit results from the $T_* = 3500$ K model, which are presented in Table 3.

The luminosity of the remnant star from the best-fit DUSTY SED models of ZTF SLRN-2020 is $L_* = 0.29^{+0.03}_{-0.06} L_\odot$. If this derived luminosity is representative of the star’s baseline output, it suggests that ZTF SLRN-2020 hosts a $\sim 0.7 M_\odot$ K-type star⁵. The low mass derived by the DUSTY analysis of the +830 d data is in rough agreement with the lower mass estimate range inferred from the IR progenitor brightness and colors by De et al. (2023) ($0.8 - 1.5 M_\odot$), who used archival data from the United Kingdom Infrared Telescope (UKIRT) Galactic plane survey (Lawrence et al. 2007). De et al. (2023) also noted that the stellar masses were not well constrained due to the photometric errors of the near-IR UKIRT progenitor photometry: $\sigma_H = 0.25$ mag and $\sigma_K = 0.18$ mag.

⁵ Assuming a mass-luminosity relation of $\left(\frac{L}{L_\odot}\right) \approx \left(\frac{M}{M_\odot}\right)^4$.

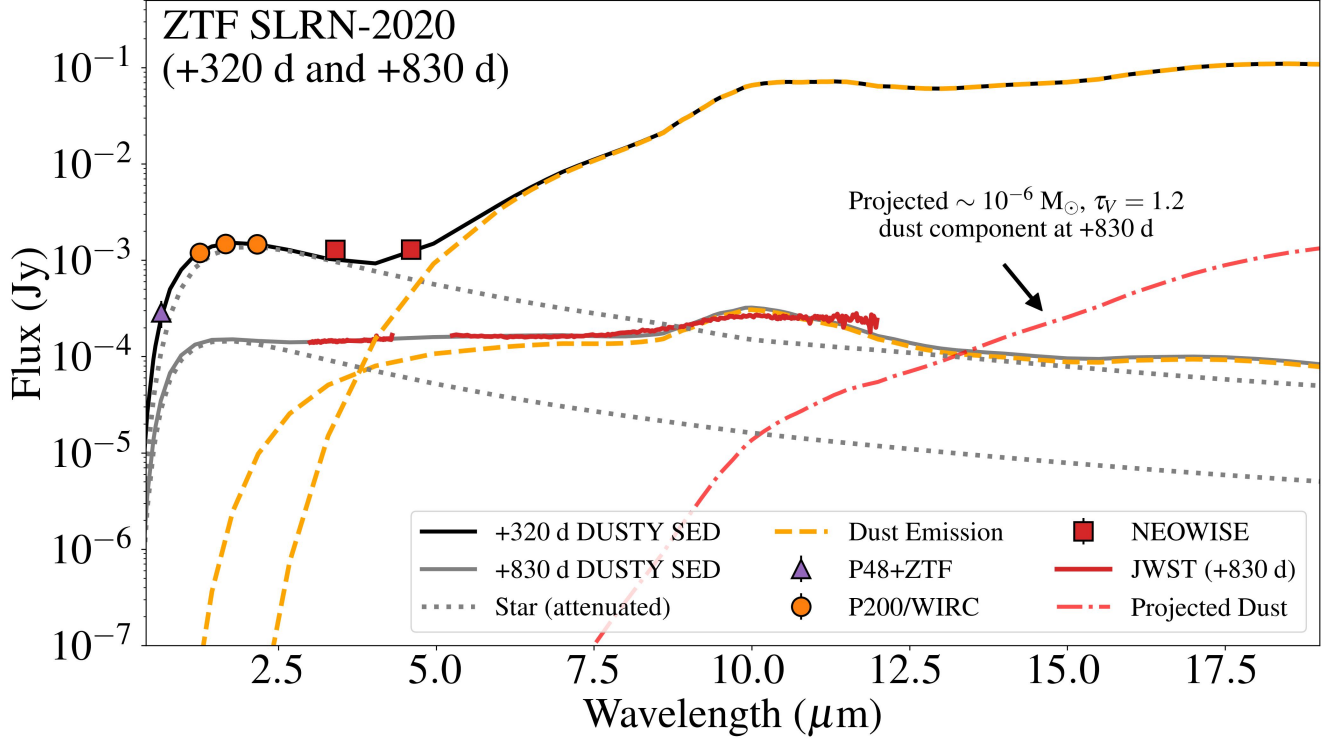


Figure 7. Best-fit DUSTY model of the ZTF SLRN-2020 SED from archival P48+ZTF, P200/WIRC, and NEOWISE data taken +320 d after the outburst peak (De et al. 2023) overlaid with the JWST (+830 d) SED and best-fit, $T_* = 3500$ K model from Figure 6. The best-fit +320 d parameters of the model are provided in Tab. 3. The dot-dashed red line shows the estimated SED of the +320 d model projected to +830 d, which assumes a dust mass of $\sim 10^{-6} M_\odot$ and an optical depth of $\tau_V = 1.2$ (See Sec. 4.1.2). This projected dust component could be undetected in the +830 d JWST observations. For clarity, the scattered-light emission component from the DUSTY models are not shown but are included in the total DUSTY SED models (solid black and grey lines).

Intriguingly, a K-type star should still be on the main-sequence, which suggests that radial expansion due to stellar evolution may not have been the mechanism that triggered the planetary engulfment event. However, it is possible that a cool and optically thick circumstellar dust component (De et al. 2023) undetected by JWST may be obscuring a fraction of the stellar luminosity. We investigate this in more detail in Sec. 4.1.1.

We derived the circumstellar dust mass of ZTF SLRN-2020 from the best-fit DUSTY SED modeling parameters (Tab. 3) and following the approach outlined in Sec. A and Eq. A5:

$$\text{Log} \left(\frac{M_d}{M_\odot} \right) \approx -10.61^{+0.08}_{-0.16}. \quad (3)$$

In the dust mass calculations, a value of $1.123 \times 10^4 \text{ cm}^2 \text{ g}^{-1}$ is adopted for the dust opacity⁶ (κ_V^d), which is consistent with the Weingartner & Draine (2001) Milky

Way grain-size distribution for $R_V = 3.1$ with dust optical properties from Draine (2003)⁷.

Assuming a gas-to-dust mass ratio of 100, we can estimate the total mass of the circumstellar material around ZTF SLRN-2020:

$$\text{Log} \left(\frac{M_{\text{CSM}}}{M_\odot} \right) \approx -8.61^{+0.08}_{-0.16}. \quad (4)$$

The circumstellar mass is notably several orders of magnitude less than the $\sim 10^{-6} M_\odot$ of material estimated by De et al. (2023) from their DUSTY SED modeling of the +320 d SED of ZTF SLRN-2020. The dust temperature and inner radius from our best-fit DUSTY model of the +830 d SED ($T_d \approx 720$ K and $R_{\text{in}} \approx 50 R_\odot$; Tab. 3) is hotter and smaller, respectively, than the values derived by De et al. (2023) from the +320 d SED, where $T_d = 415$ K and $R_{\text{in}} = 1140 R_\odot$. The less massive, hotter, and more close-in circumstellar material derived from the +830 d epoch compared to that of the +320 d

⁶ the dust absorption cross section weighted by dust mass

⁷ https://www.astro.princeton.edu/~draine/dust/extcurvs/kext_albedo_WD_MW_3.1_60_D03.all

epoch may therefore be a distinct circumstellar component surrounding the remnant star that was not revealed by the +320 d SED (De et al. 2023).

3.4. Revisiting the +320 d SED Modeling

In order to investigate the evolving properties of ZTF SLRN-2020 between the +320 d epoch reported by De et al. (2023) and the +830 d epoch from this work, we revisit the +320 d SED using a consistent DUSTY modeling approach that we performed for the +830 d epoch. Utilizing the photometry from *r*-band through W2 (i.e. $\lambda = 0.64 - 4.6 \mu\text{m}$) reported by De et al. (2023) from the +320 d epoch, we conducted a grid search across the inner boundary dust temperature T_d , the optical depth of the circumstellar dust shell τ_V , and the effective temperature of the heating source T_* . Note that in this analysis of the +320 d SED, the effective temperature was included as a grid-search parameter due to the better wavelength coverage of the heating source compared to that of the +830 d observations. We also adopt the same grain size and composition parameters as the +830 d model: an MRN distribution with minimum and maximum grain sizes of $0.005 \mu\text{m}$ and $0.25 \mu\text{m}$, respectively, a grain-size power-law index of -3.5 , and a 50/50 silicate/amorphous-carbon composition.

In the +320 d DUSTY grid search, the values for T_d ranged from 100–1000 K with a step size of 25 K, the values for τ_V ranged from 0.2–15 with a step size of 0.4, and the values for T_* ranged from 2600–7000 K with a step size of 200 K. Figure 7 shows the resulting best-fit model for the +320 d SED and the +830 d SED model for comparison. The best-fit SED model parameters are provided in Table 3.

The luminosity of ZTF SLRN-2020 was notably a factor of $\gtrsim 10$ greater at +320 d, when ZTF SLRN-2020 was still in outburst, than at +830 d. The rapid decrease in luminosity deviates from the predicted $L_* \propto t^{-4/5}$ power-law decay for the gravitational contraction of an inflated host star envelope following the engulfment (Tylenda et al. 2005; De et al. 2023).

The dust mass of the ZTF SLRN-2020 ejecta probed by the +320 d SED, $\text{Log}\left(\frac{M_d}{M_\odot}\right) = -5.89^{+0.29}_{-3.21}$, implies a total ejecta mass of

$$\text{Log}\left(\frac{M_{\text{ej}}}{M_\odot}\right) = -3.89^{+0.29}_{-3.21} \quad (5)$$

assuming a gas-to-dust mass ratio of 100. Although the best-fit model parameters for the +320 d exhibits large uncertainties due to the limited mid-IR wavelength coverage out to $4.6 \mu\text{m}$, the results suggest that there is a more extended, cooler, and more massive circumstellar

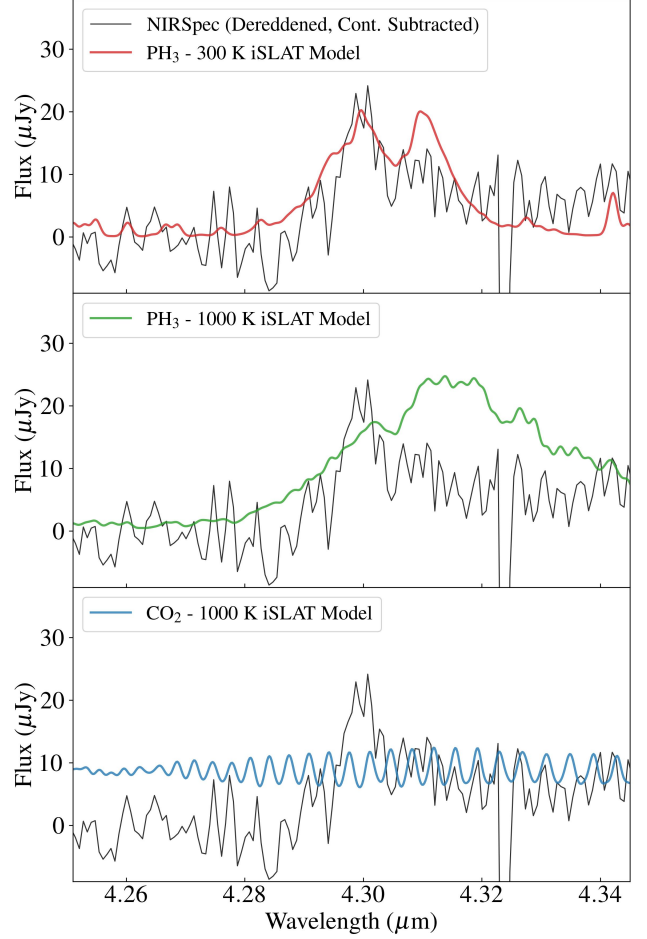


Figure 8. Synthetic iSLAT spectra of (Top) PH_3 at 300 K, (Middle) PH_3 at 1000 K, and (Bottom) CO_2 at 1000 K overlaid on the dereddened and continuum-subtracted JWST/NIRSpec spectrum of ZTF SLRN-2020. The 300 K PH_3 model presents the closest agreement with the NIRSpec spectrum.

component and a closer-in, hotter, and less massive component. We note that the implied total ejecta mass of $\sim 10^{-4} M_\odot$ ($\approx 0.1 M_{\text{Jup}}$) is consistent with the inferred ejecta mass based on the luminosity and duration of the ZTF SLRN-2020 outburst (Matsumoto & Metzger 2022; De et al. 2023).

3.5. Possible detection of Phosphine (PH_3)

Based on an analysis with the interactive Spectral-Line Analysis Tool (iSLAT, Jellison et al. 2024), we attributed the broad emission feature revealed by NIRSpec at $\sim 4.3 \mu\text{m}$ to PH_3 ⁸. Synthetic spectra of PH_3 at temperatures consistent with warm (1000 K) and cool

⁸ iSLAT model spectra were convolved with a Gaussian with a FWHM of 120 km s^{-1} to match the resolving power of the NIRSpec observations.

(300 K) models were generated from iSLAT using a simple slab model and molecular data from HITRAN (Gordon et al. 2022). The synthetic PH_3 spectra are shown in Figure 8 overlaid on the dereddened and continuum-subtracted $\sim 4.3 \mu\text{m}$ feature. Since CO_2 has a prominent band that overlaps with the $\sim 4.3 \mu\text{m}$ PH_3 band, we also generated a synthetic spectrum of CO_2 to rule it out as the origin of the feature (Fig. 8). Neither the 1000 K PH_3 model nor the CO_2 model resemble the $\sim 4.3 \mu\text{m}$ feature; however, the 300 K PH_3 model shows a general agreement with the feature.

The 300 K PH_3 iSLAT model assumed a radius of 22 au, consistent with the inner radius of the best-fit DUSTY model of the ejecta dust (i.e. the dust component revealed at +320 d; Tab. 3). A column density of $N_{\text{PH}_3} \sim 2 \times 10^{15} \text{ cm}^{-2}$ was derived by approximately scaling the amplitude of the synthetic feature to that of the observed feature. If the emitting PH_3 is indeed located in the ejecta, we can estimate the PH_3 mass and the abundance of PH_3 relative to H_2 assuming that the total gas mass of the ejecta ($M_{\text{ej}} \sim 10^{-4} M_\odot$; See Eq. 5) is dominated by H_2 . The approximate PH_3 mass is

$$N_{\text{PH}_3} \times \pi R_{\text{PH}_3}^2 \times m_{\text{PH}_3} \sim 2 \times 10^{-11} M_\odot \quad (6)$$

and the abundance of PH_3 relative to H_2 is approximately

$$\frac{N_{\text{PH}_3} \times \pi R_{\text{PH}_3}^2}{M_{\text{ej}}/m_{\text{H}_2}} \sim 10^{-8} \quad (7)$$

where m_{H_2} is the mass of an H_2 molecule, m_{PH_3} is the mass of a PH_3 molecule, and R_{PH_3} ($= 22 \text{ au}$) is the assumed radius of the PH_3 emitting region. Interestingly, the abundance of PH_3 relative to H_2 from ZTF SLRN-2020 is consistent with that of the circumstellar material around the AGB star IRC +10216 (Agúndez et al. 2014). The molecular outflows from ZTF SLRN-2020 and stellar mergers notably exhibit similar molecular features as the cool envelopes of red, evolved stars (Kamiński et al. 2018; De et al. 2023), which suggests similar conditions for PH_3 formation. The consistent relative PH_3 abundances provides further evidence that the $\sim 4.3 \mu\text{m}$ feature from ZTF SLRN-2020 is indeed associated with PH_3 .

4. DISCUSSION

4.1. Investigating the Remnant Host Star and its Circumstellar Environment

There are two prevailing and related questions arising from the newly obtained +830 d observations from JWST and the re-analysis of the +320 d SED from De et al. (2023):

- Does ZTF SLRN-2020 host a $\sim 0.7 M_\odot$ K-type star that should not have evolved off the main sequence yet or is the stellar luminosity obscured by cooler circumstellar dust?
- Could $\sim 10^{-6} M_\odot$ of dust ($\approx 10^{-4} M_\odot$ of total gas+dust mass) produced by ZTF SLRN-2020 have gone undetected by the JWST observations?

These questions are related because the high dust mass component from the +320 d SED model, which is notably absent from the +830 d SED model, may be responsible for blocking a significant fraction of the remnant star luminosity. In this section, we address these two questions and discuss the implications of our results.

4.1.1. Is a More Luminous Remnant Star Obscured by Cool Circumstellar Dust?

We assess if ZTF SLRN-2020 might host a more luminous star that could be evolving off the main sequence (e.g. $L_* \gtrsim 1 L_\odot$) when accounting for additional obscuration from the $\sim 10^{-6} M_\odot$ dust component identified in the +320 d SED but undetected at +830 d (See Tab. 3). Given the measured luminosity of $L_* = 0.29 L_\odot$ from the +830 d SED model, $\gtrsim 70\%$ of a $\gtrsim 1 L_\odot$ source would have to be obscured by the undetected dust component. In order to estimate the level of obscuration, we project the +320 d dust optical depth ($\tau_V^{+320\text{d}} = 4.2$) out to +830 d assuming a constant dust expansion velocity of

$$v_{\text{exp}} \approx R_{\text{in}}^{+320\text{d}}/320 \text{ d} \approx 120 \text{ km s}^{-1} \quad (8)$$

Based on Equations A1 & A2, the optical depth can be estimated as follows:

$$\tau_V^{+830\text{d}} \approx \tau_V^{+320\text{d}} \frac{Y^{+320\text{d}} R_{\text{in}}^{+320\text{d}}}{(R_{\text{in}}^{+320\text{d}} + \Delta t v_{\text{exp}})(Y^{+320\text{d}} R_{\text{in}}^{+320\text{d}} + \Delta t v_{\text{exp}})}, \quad (9)$$

where $Y^{+320\text{d}}$ is the shell thickness factor in the +320 d DUSTY models that was assumed to be 5, Δt is the time elapsed between the +320 d and +830 d observations (i.e. $\Delta t = 510 \text{ d}$), and $R_{\text{in}}^{+320\text{d}}$ is the inner radius of $\sim 10^{-6} M_\odot$ dust component in the +320 d SED model (Tab. 3). We therefore estimate that the optical depth of the $\sim 10^{-6} M_\odot$ component at +830 d would be

$$\tau_V^{+830\text{d}} \sim 1.2. \quad (10)$$

Adopting a Weingartner & Draine (2001) extinction curve with $\tau_V = 1.2$ for the circumstellar dust, we calculate that the dust component would obscure $\approx 32 - 46\%$ of the stellar luminosity for a source with an effective temperature ranging from 3500 – 5000 K. Based on the best-fit $0.29 L_\odot$ luminosity from the +830 d model

(Tab. 3), the dust-corrected luminosity of the remnant star would be $L_*^{\text{cor}} \approx 0.4 L_\odot$ for an effective temperature of $T_* = 3500$ K and $L_*^{\text{cor}} \approx 0.5 L_\odot$ for an effective temperature of $T_* = 5000$ K.

The stellar luminosities that have been corrected for possible obscuration from a $10^{-6} M_\odot$, $\tau_V = 1.2$ circumstellar dust shell are notably still consistent with a K-type star with a mass $\lesssim 0.85 M_\odot$. Note that these dust-corrected luminosities also agree with the lower-mass range estimated by the IR progenitor brightness and color analysis by De et al. (2023): $0.8 - 1.5 M_\odot$. These results demonstrate even if the ZTF SLRN-2020 host star is obscured by an undetected $\sim 10^{-6} M_\odot$ of dust at +830 d, it is unlikely the host is massive enough to have left the main sequence. We suggest that the ZTF SLRN-2020 planetary engulfment event was not triggered by radial expansion from stellar evolution.

4.1.2. Observational Constraints on a $\sim 10^{-6} M_\odot$ Circumstellar Dust Component at +830 d

Based on our DUSTY SED analysis (Sec. 3.3) and JWST observations, we can estimate constraints on the physical parameters of the ZTF SLRN-2020 ejecta. Specifically, we address if the $\sim 10^{-6} M_\odot$ dust component from the ZTF SLRN-2020 ejecta identified in the +320 d analysis could have been undetected in the late-time, +830 d JWST observations.

We utilize DUSTY to model the predicted emission from a $\sim 10^{-6} M_\odot$, $\tau_V = 1.2$ dust component at +830 d and then compare against the +830 d JWST observations. Instead of adopting the best-fit +830 d heating source parameters (Tab. 1), which may be obscured by undetected circumstellar dust, we adopt the dust-corrected star model with $L_* = 0.5 L_\odot$ and $T_* = 5000$ K from Sec. 4.1.1. We note that an effective temperature of 5000 K is also inferred for the ZTF SLRN-2020 host star by De et al. (2023). The projected shell thickness factor for the $\sim 10^{-6} M_\odot$ component can be estimated as $Y^{+830d} = \frac{Y^{+320d} R_{\text{in}}^{+320d} + \Delta t v_{\text{exp}}}{R_{\text{in}}^{+320d} + \Delta t v_{\text{exp}}} \approx 2.5$.

The dust temperature at the inner radius of the $\sim 10^{-6} M_\odot$ component at +830 d must then be estimated as the final input needed for the DUSTY model. The temperature of this dust component can be estimated at the time of the +830 d observations assuming it is in radiative equilibrium with the radiation field from the central remnant star. Following the equilibrium temperature description in Sec. B and adopting a dust emissivity power-law index of $\beta = 1$, the projected dust temperature of the $\sim 10^{-6} M_\odot$ dust component at +830 can be estimated as follows:

$$T_d^{+830d} \approx T_d^{+320d} \left(\frac{\langle Q_{\text{abs}} \rangle_*^{+830d}}{\langle Q_{\text{abs}} \rangle_*^{+320d}} \right)^{1/5} \left(\frac{L_*^{+830d}}{L_*^{+320d}} \right)^{1/5} \left(\frac{r^{+830d}}{r^{+320d}} \right)^{-2/5}, \quad (11)$$

where $\langle Q_{\text{abs}} \rangle_*$ is the spectrum-averaged absorption cross section, L_* is the central heating source luminosity, and r is the separation distance between dust and the heating source. The radius of the $\sim 10^{-6} M_\odot$ dust component at +830 d can be estimated as $r^{+830d} \approx R_{\text{in}}^{+320d} + \Delta t v_{\text{exp}} \approx 12330 R_\odot$, and the heating source luminosity is assumed to be $L_*^{+830d} = 0.5 L_\odot$. The values for $\langle Q_{\text{abs}} \rangle_*$ of the heating source at +320 d and +830 d can be estimated using Eq. B8 for effective temperatures $T_*^{+320d} = 5800$ K (Tab. 3) and $T_*^{+830d} = 5000$ K. Since the effective temperatures are not too different, we find that $\left(\frac{\langle Q_{\text{abs}} \rangle_*^{+830d}}{\langle Q_{\text{abs}} \rangle_*^{+320d}} \right)^{1/5} \approx 1.0$ for silicate and carbonaceous dust grains. Using the above parameters and the best-fit model values for $T_d^{+320d} = 280$ K, $L_*^{+320d} = 13 L_\odot$, and $r^{+320d} = 4730 R_\odot$, we estimate a projected inner-radius dust temperature of

$$T_d^{+830d} \approx 100 \text{ K} \quad (12)$$

for the $\sim 10^{-6} M_\odot$, $\tau_V = 1.2$ dust component at +830 d.

With the input parameters provided above, we generate a DUSTY dust emission model of the $\sim 10^{-6} M_\odot$ dust component. The amplitude of the dust emission SED output from DUSTY is appropriately scaled by normalizing the total integrated stellar emission to $0.5 L_\odot$ at a distance of 4 kpc to ZTF SLRN-2020. As shown in Fig. 7, the projected emission from the $\sim 10^{-6} M_\odot$ dust component is lower than the dereddened emission covered by the JWST MIRI/LRS observations. The observational constraints from JWST therefore indicate that in addition to the warmer ($T_d = 720$ K) and less massive ($M_d \sim 10^{-11} M_\odot$) dust component revealed from the +830 d SED modeling, up to $\sim 10^{-6} M_\odot$ of cool dust formed in the ZTF SLRN-2020 ejecta may also be present in the circumstellar environment of the remnant star.

In Sec. C, we conduct a similar analysis using the +320 d circumstellar dust parameters derived by De et al. (2023) and conclude that the parameters from our +320 d best-fit DUSTY model are more consistent with the observational constraints.

4.1.3. Interpreting the Warm Dust Component as Ejecta Fallout

We suggest that the warm, $\sim 10^{-11} M_\odot$ dust component revealed by JWST may have originated from fallback from part of the ejecta (e.g. MacLeod et al. 2018b).

Dust condensed from the ejecta is likely traced by the cooler $\sim 10^{-6} M_{\odot}$ dust component observed at +320 d, especially given the evolution of this dust component throughout the ZTF SLRN-2020 outburst reported by De et al. (2023). The fallback interpretation is plausible given that the inferred ejecta velocity ($\sim 100 \text{ km s}^{-1}$) is less than the estimated escape velocity of $v_{\text{esc}} \sim 300 \text{ km s}^{-1}$ (De et al. 2023). Given the detections of ^{12}CO and $\text{Br}\alpha$ emission (Fig. 2), the warm and dusty circumstellar material may also be configured in an accretion disk around the remnant star as shown in Fig. 9 (Right). Another possible interpretation of the warm $\sim 10^{11} M_{\odot}$ dust component may be a super-Eddington wind driven by energy deposition near the surface of the host star from the planetary engulfment (e.g. Quataert et al. 2016). However, De et al. (2023) measure a peak luminosity from ZTF SLRN-2020 ($\sim 10^{35} \text{ erg s}^{-1}$) that is well below the Eddington luminosity for a $\sim 1 M_{\odot}$ star.

We can investigate the ejecta fallback interpretation for the warm circumstellar dust component assuming the observed $\text{Br}\alpha$ emission (Fig. 3) arises from accretion of fallback ejecta on the remnant star. We assess whether or not the warm dust component, which has a total circumstellar mass of $M_{\text{CSM}} \sim 10^{-9} M_{\odot}$ (Eq. 4), provides a sufficient mass reservoir to power the observed $\text{Br}\alpha$ line luminosity.

Based on the $\text{Br}\alpha$ line flux from the Gaussian profile fit (Tab. 2) and adopting a distance of 4 kpc to ZTF SLRN-2020, the $\text{Br}\alpha$ luminosity is

$$L_{\text{Br}\alpha} \sim 10^{-5} L_{\odot} \quad (13)$$

The luminosity of hydrogen recombination lines have notably been used as proxies for accretion luminosity for systems such as T Tauri stars (e.g. Salyk et al. 2013), a class of young and accreting low-mass ($M_{*} < 2 M_{\odot}$) stars. The hydrogen emission lines from T Tauri stars are thought to originate from the accretion columns and accretion shock (Calvet & Gullbring 1998). Assuming a similar mechanism is driving the $\text{Br}\alpha$ emission for the ZTF SLRN-2020 remnant star, we estimate L_{acc} from $L_{\text{Br}\alpha}$ by adopting the empirical $L_{\text{Br}\alpha}$ - L_{acc} relation derived for T Tauri stars (Komarova & Fischer 2020):

$$\text{Log} \left(\frac{L_{\text{acc}}}{L_{\odot}} \right) = (1.81 \pm 0.11) \text{Log} \left(\frac{L_{\text{Br}\alpha}}{L_{\odot}} \right) + (6.45 \pm 0.38). \quad (14)$$

Based on Eq. 14, we infer an accretion luminosity for the remnant star of ZTF SLRN-2020,

$$L_{\text{acc}} \sim 4 \times 10^{-3} L_{\odot}. \quad (15)$$

From the accretion luminosity, we can approximate the remnant star's mass accretion rate, \dot{M}_{acc} , given the following relation

$$L_{\text{acc}} \approx G M_{*} \dot{M}_{\text{acc}} / R_{*}, \quad (16)$$

where M_{*} is the mass of the remnant star, R_{*} is the radius of the remnant star, and G is the gravitational constant. Assuming $\frac{M_{*}}{R_{*}} \sim \frac{M_{\odot}}{R_{\odot}}$, we estimate a mass accretion rate of

$$\dot{M}_{\text{acc}} \sim 10^{-10} M_{\odot} \text{ yr}^{-1}. \quad (17)$$

The $\sim 10^{-9} M_{\odot}$ of warm circumstellar material (Eq. 4) indeed provides a sufficient mass reservoir to power the estimated mass accretion rate and therefore supports the interpretation of the warm dust component as fallback from the ejecta.

4.2. Addressing the Nature of ZTF SLRN-2020

Our JWST results and analysis indicate that the luminosity of the ZTF SLRN-2020 remnant host star is consistent with a K-type main-sequence star even if it were obscured by $10^{-6} M_{\odot}$ of ejecta dust (Sec. 3.3.1 & 4.1.1). The properties of the remnant star should reflect that of the progenitor since the remnant star has likely relaxed to its normal state based on the stability of its near-IR emission (Fig. 2). ZTF SLRN-2020 was therefore unlikely triggered by radial expansion from stellar evolution since the main sequence lifetime for K-type stars ($\gtrsim 15 \text{ Gyr}$) is longer than the age of the Universe. In this section, we discuss the implications of our results and the persisting questions on the nature of ZTF SLRN-2020 planetary engulfment event.

We raise an important caveat on the measured stellar luminosity arising from the uncertainty on the estimated distance to ZTF SLRN-2020. Based on an a comparative analysis of extinction maps, De et al. (2023) claim $d = 4 \text{ kpc}$ is the best distance estimate for the source but indicate a conservative distance range of 2 – 7 kpc. Given our $L_{*} \approx 0.3 L_{\odot}$ calculation for the host star luminosity (Tab. 3), the upper-bound distance would imply a stellar luminosity and mass of $\approx 0.9 L_{\odot}$ and $\approx 1 M_{\odot}$, respectively, and such a star may have been evolving off of the main sequence. However, the three Galactic dust extinction maps (Drimmel et al. 2003; Marshall et al. 2006; Green et al. 2019) used by De et al. (2023) to estimate the distance show consistent overlaps between the range of $\approx 3 - 4 \text{ kpc}$, which motivated adopting 4 kpc as the best distance estimate towards ZTF SLRN-2020.

4.2.1. Engulfment triggered by orbital decay via tidal interactions?

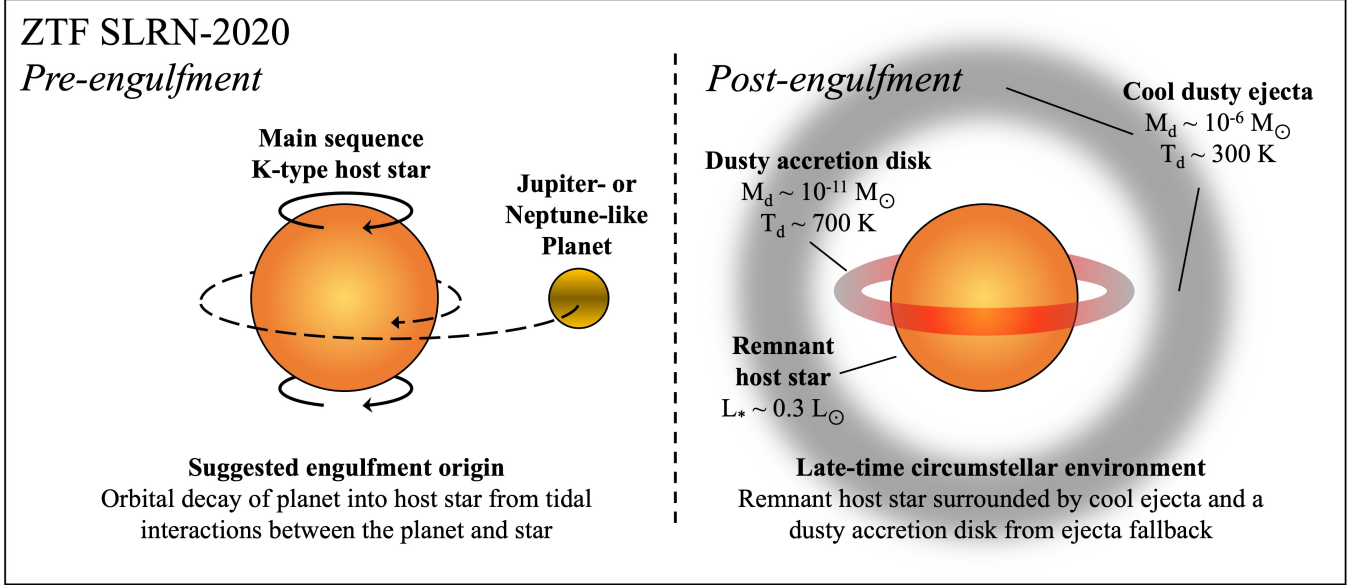


Figure 9. Schematic illustration of the pre- and post-engulfment interpretation of ZTF SLRN-2020. (*Left*) The $\sim 0.3 L_\odot$ luminosity of the ZTF SLRN-2020 remnant host star from DUSTY SED modeling (Sec. 3.3.1, Tab. 3) is consistent with a K-type main sequence star. ZTF SLRN-2020 was therefore unlikely triggered by radial expansion from stellar evolution (Sec. 4.2). Engulfment may instead be triggered by orbital decay of planet into the host from tidal interactions (Sec. 4.2.1). (*Right*) At late times (+830 d), the remnant host star may be surrounded by dusty accretion disk composed of fallback from the ejecta (Sec. 4.1.3). Ejecta dust detected by previous observations at +320 d (Sec. 3.4) is not detected by JWST at +830 d because the ejecta dust may have cooled beyond detection limits and wavelength coverage of observations (Sec. 4.1.2).

If ZTF SLRN-2020 was not caused by stellar evolution, a plausible hypothesis for the mechanism that triggered the planetary engulfment event is tidal interactions between the host star and the planet companion (See Fig. 9, *Left*). Such interactions can lead to an orbital decay of the planet into the host star as energy and angular momentum are transferred from the orbit of the planet to the host star (e.g. Zahn 1977; Jackson et al. 2009). Evidence of orbital decay from tidal interactions has notably been provided from transit-timing observations of the hot Jupiters WASP-12b (Maciejewski et al. 2016; Patra et al. 2020; Yee et al. 2020) and Kepler-1658b (Vissapragada et al. 2022). Hamer & Schlaufman (2019) also argue that hot Jupiters are destroyed by tides during the main-sequence lifetimes of their host stars based on a Galactic velocity dispersion study of stars with and without hot Jupiters. The orbital decay timescales based on recent simulations for host stars $\lesssim 1 M_\odot$ and planets with an orbital period $\lesssim 1$ day are $< 10^8$ yr (Weinberg et al. 2024), which is notably much shorter than the main-sequence lifetime of a K-type star.

Other mechanisms that could lead to planetary engulfment include planet-planet scattering (Rasio & Ford 1996; Chatterjee et al. 2008; Carrera et al. 2019) and gravitational perturbations from another companion (Holman et al. 1997; Naoz et al. 2012; Stephan et al. 2018). These mechanisms could excite high orbital ec-

centricities such that interactions between the planet and the host star might occur at periape, though De et al. (2023) argue that ZTF SLRN-2020 must have had a nearly-circular orbit by the time the planet was engulfed due to the steadily rising pre-outburst luminosity. We therefore favor the orbital decay scenario. However, observations of additional planetary engulfment events will be crucial for assessing the dominant mechanism(s).

4.2.2. Engulfment or Tidal Disruption?

Understanding the nature of the host star can provide insight into the physics behind ZTF SLRN-2020. In particular, the ratio of the mean densities of the planet and host star is thought to be a proxy for the outcome of the star-planet interaction (Metzger et al. 2012). A K-type main sequence star has a mean stellar density of $\bar{\rho}_* \sim 3 \text{ g cm}^{-3}$, which is greater than that of hot Jupiters that tend to be “inflated” (Baraffe et al. 2010) and exhibit relatively low mean densities ($\bar{\rho}_p \lesssim 1 \text{ g cm}^{-3}$). Instead of being fully engulfed, which should occur when the mean density of the planet is greater than that of the host star, a planet with a mean density lower than that of their host star may undergo tidal disruption near or above the stellar surface. Tidal disruption of the planet would lead to the formation of an accretion disk that can drive outflows from super-Eddington accretion onto the host star (Metzger et al. 2012; Matsumoto & Metzger 2022).

Alternatively, given the Neptune-like ($\sim 0.1 M_{\text{Jup}}$) lower-end mass estimate of the engulfed companion by De et al. (2023)⁹, we speculate that perhaps the engulfed planet from ZTF SLRN-2020 was in the “Hot Neptune Desert” (Szabó & Kiss 2011). Among the handful of known planets in the Hot Neptune Desert, several exhibit mean densities of $\bar{\rho}_p \gtrsim 3 \text{ g cm}^{-3}$ (e.g. Armstrong et al. 2020; Naponiello et al. 2023; Nabbie et al. 2024). A “hot Neptune” could therefore be engulfed by a K-type main-sequence host star. However, since such planets appear to be relatively rare compared to hot Jupiters, the star-planet interaction leading to ZTF SLRN-2020 more likely involved a hot Jupiter than a hot Neptune.

The physics that ultimately drive the mass ejection in tidal disruption scenario is distinct from the engulfment scenario where the planet deposits its orbital energy into its surroundings as it plunges into the host star (MacLeod et al. 2018a). Signatures of chemical enrichment of the host star from the planet may differ for each scenario since ejecta from a merger/engulfment should be dominated by material from the host star envelope (Metzger et al. 2012; Matsumoto & Metzger 2022), whereas the accretion disk from tidal disruption will be composed of the planetary material (Metzger et al. 2012). Both scenarios, however, can result in a transient outburst with potentially similar observational properties (e.g. Bear et al. 2011; Soker 2023). Spectroscopic follow-up of ZTF SLRN-2020 searching for signatures of chemical enrichment may help distinguish its origin as well as provide a valuable dataset for investigating anomalous stellar chemical compositions, which indicate at least one in a dozen stars presents evidence of planet engulfment (Liu et al. 2024).

Given the similarities of ZTF SLRN-2020 to other engulfment/merger-powered red novae (De et al. 2023), such as the presence of multiple dust components (e.g. Tyllenda & Kamiński 2016; Woodward et al. 2021), we favor the engulfment interpretation for ZTF SLRN-2020. We also note that although hot Jupiters tend to possess relatively low mean densities, hot Jupiters with mean densities $\bar{\rho}_p \gtrsim 3 \text{ g cm}^{-3}$ are known to exist (e.g. Deleuil et al. 2012; Rouan et al. 2012; Espinoza et al. 2017). We acknowledge that the $\bar{\rho}_p/\bar{\rho}_* < 1$ mean density ratio between a K-type star and a typical hot Jupiter-like planet as well as the deviation from the $L_* \propto t^{-4/5}$ power-law decay expected for

a merger/engulfment event (Sec. 3.4) present open questions on the engulfment interpretation. Further theoretical/simulation work on star-planet interactions (e.g. Lau et al. 2022; Yarza et al. 2023) in addition to multi-wavelength observations of more subluminal red novae like ZTF SLRN-2020 will be important for distinguishing the physics that drive these transient events.

5. SUMMARY AND CONCLUSIONS

In this paper, we presented late-time (+830 d) spectroscopic IR observations of the planetary engulfment event ZTF SLRN-2020 with JWST/NIRSpec and MIRI. The $\sim 3 - 12 \mu\text{m}$ spectra from JWST were complemented with near-contemporaneous, near-IR photometry from ground-based imaging with Gemini-N/NIRI (Fig. 2). In our analysis of the $\sim 1 - 12 \mu\text{m}$ SED of ZTF SLRN-2020, we also incorporated previously published near-IR photometry from P200/WIRC taken a few weeks before the Gemini-N observations (De et al. 2023). A schematic illustration of the pre- and post-engulfment interpretation of ZTF SLRN-2020 that summarizes the main results and implications is shown in Figure 9).

The $\sim 1 - 12 \mu\text{m}$ observations of ZTF SLRN-2020 likely trace emission from the remnant host star in the near-IR and thermal dust emission at longer wavelengths in the mid-IR. We identified the following notable properties from the dereddened $\sim 1 - 12 \mu\text{m}$ SED: a peak in the near-IR around the H -band, the detection of Br α emission, the potential detection of PH $_3$ emission at $\sim 4.3 \mu\text{m}$, and the presence of ^{12}CO fundamental band emission at $\sim 4.7 \mu\text{m}$. Interestingly, ^{12}CO emission was also detected around the red nova V4332 Sgr (Banerjee et al. 2004), which has been compared to ZTF SLRN-2020 due to its low luminosity (De et al. 2023). The detections of ^{12}CO fundamental band and Br α emission suggest the presence of hot circumstellar gas that may be accreting onto the host star.

We modeled the ^{12}CO emission from ZTF SLRN-2020 using `spectools_ir` which revealed hot ($T_{\text{CO}} \sim 1340 \text{ K}$) and close-in ($R_{\text{CO}} \sim 15 R_{\odot}$) circumstellar gas with a total CO mass of $\text{Log} \left(\frac{M_{\text{CO}}}{M_{\odot}} \right) \approx -13.1^{+0.3}_{-0.3}$ (Fig. 4, Tab. 3). Based on the CO gas mass, we estimated a total gas mass of $\text{Log} \left(\frac{M_{\text{gas}}}{M_{\odot}} \right) \approx -10.2^{+0.3}_{-0.3}$. Although the ^{12}CO fundamental band in emission is typically detected from YSOs, Herbig Ae/Be stars, and T Tauri disks, the observed properties of ZTF SLRN-2020 presented in this work and by De et al. (2023) conflict with these interpretations. The JWST spectra are therefore consistent with the claim that ZTF SLRN-2020 arose from a planetary engulfment event.

⁹ The $0.1 M_{\text{Jup}}$ mass estimate was derived from linearly scaling the companion mass in the stellar merger V1309 Sco (Tyllenda et al. 2011) based on the ejecta mass and radiated energy of V1309 Sco and ZTF SLRN-2020.

We analyzed the broad emission feature at $\sim 4.3 \mu\text{m}$ with synthetic spectral models from iSLAT and attributed the feature to PH_3 . The analysis suggests the presence of $\sim 2 \times 10^{-11} M_\odot$ of 300 K PH_3 assuming it is co-spatial with the circumstellar material at a distance of 22 au from the remnant host star. The abundance of PH_3 relative to H_2 is approximately $\sim 10^{-8}$, which is notably consistent with that of the circumstellar material around the AGB star IRC +10216 (Agúndez et al. 2014).

We investigated the properties of the ZTF SLRN-2020 remnant host star and circumstellar dust by fitting DUSTY radiative transfer models. Based on the best-fit model to the late-time (+830 d) $1 - 12 \mu\text{m}$ SED, we derived a luminosity of $L_* \approx 0.3 L_\odot$ for the surviving host star, which is consistent with a $\sim 0.7 M_\odot$ K-type star. From the late-time, +830 d SED, we derived a circumstellar dust mass of $\text{Log}\left(\frac{M_d}{M_\odot}\right) \approx -10.61^{+0.08}_{-0.16}$ and dust temperature of $T_d = 720$ K. Assuming a gas-to-dust mass ratio of 100, we estimated a total circumstellar mass of $\text{Log}\left(\frac{M_{\text{CSM}}}{M_\odot}\right) \approx -8.61^{+0.08}_{-0.16}$. The circumstellar dust component revealed from the +830 d SED may therefore be distinct from the cooler and more massive component probed by the +320 d SED from De et al. (2023). In order to investigate this, we re-analyzed the +320 d SED using a similar grid-search approach as the +830 d SED analysis with DUSTY (Fig. 7). Our revised analysis of the +320 d SED provided a total dust mass of $\text{Log}\left(\frac{M_d}{M_\odot}\right) = -5.89^{+0.29}_{-3.21}$ and dust temperature of $T_d \sim 280$ K (Tab. 3). We therefore suggested that the remnant star of ZTF SLRN-2020 has at least two distinct circumstellar dust components.

Given the likely presence of a cool, massive circumstellar dust shell around the remnant star of ZTF SLRN-2020, which was not revealed by the best-fit +830 d SED model, we addressed:

- How might this impact our +830 d SED model hypothesis that ZTF SLRN-2020 hosts a $\sim 0.7 M_\odot$ K-type star.
- Whether such a massive but cool circumstellar dust component could have been missed by the JWST observations.

When factoring in the obscuration from a projected $\sim 10^{-6} M_\odot$ dust component at the +830 d epoch, our analysis indicated that the dust-corrected luminosity of the remnant star would still be consistent with a K-type star with a mass $\lesssim 0.85 M_\odot$. Given that such a star should not have evolved off of the main sequence, we suggest that the planetary engulfment event associated

with ZTF SLRN-2020 was not likely triggered by radial expansion from stellar evolution.

In order to address whether the JWST could have missed a cool circumstellar dust component, we modeled the predicted emission from the $\sim 10^{-6} M_\odot$ dust component at the +830 d epoch. As shown in Fig. 7, we determined that $\sim 10^{-6} M_\odot$ of circumstellar dust formed in the ZTF SLRN-2020 ejecta could indeed have been undetected by the +830 d JWST observations. Given that the cooler and more massive dust component likely condensed in the ejecta of ZTF SLRN-2020 (De et al. 2023), we hypothesize that the warmer dust component revealed by the JWST observations traces fallback from the ejecta and is being accreted on the remnant host star. In support of this hypothesis, we calculated that the $\sim 10^{-9} M_\odot$ of total material in the warm circumstellar component can provide a sufficient mass reservoir to power the $\sim 10^{-10} M_\odot \text{ yr}^{-1}$ mass accretion rate derived from the Br α emission line luminosity.

If ZTF SLRN-2020 was not triggered by stellar evolution, we favor the hypothesis that the planetary engulfment was due to orbital decay caused by tidal interactions between the planet and the host star. Other possible mechanisms include planet-planet scattering and gravitational perturbations from another companion. However, those two mechanisms excite high orbital eccentricities, which is not consistent with the nearly-circular orbit inferred for the system by De et al. (2023).

Lastly, we considered the implications on the star-planet interaction leading to ZTF SLRN-2020 if the host is a main-sequence K-type star. Since the mean density of the star would be greater than that of a hot Jupiter-like planet, the planet may be tidally disrupted near or above the surface of the star rather than being fully engulfed. Noting that a Neptune-like $\sim 0.1 M_{\text{Jup}}$ planet was also consistent for the engulfed companion (De et al. 2023), we speculated that the planet may have been a Hot Neptune, which exhibit higher mean densities than Hot Jupiters. Ultimately, we continue to favor the engulfment interpretation for ZTF SLRN-2020. The discovery and follow-up of new planetary engulfment events will be important for investigating the physics of these IR-luminous transient events. This study of ZTF SLRN-2020 highlights the scientific potential of coordinated IR-bright transient discovery and follow-up observations with JWST and upcoming survey facilities like the Vera C. Rubin Observatory.

We thank our JWST program coordinator Shelly Meyett for facilitating our Target of Opportunity (ToO) Activation Request, which was one of the first ToO triggers with JWST. We also thank Sarah Kendrew for the

valuable feedback on the reduction and analysis of the MIRI LRS observations. We also thank Greg Sloan for his review and feedback on our offset target acquisition strategy for the MIRI LRS observations. RML would like to acknowledge Joan Najita, J.J. Zanazzi, and Viraj Karambelkar for enlightening discussions on circumstellar disks, planetary engulfment events, and stellar mergers. RML also thanks Sarah Logsdon and Everett Schlawin for the helpful discussions on exoplanets.

This work is based on observations made with the NASA/ESA/CSA James Webb Space Telescope. The data were obtained from the Mikulski Archive for Space Telescopes at the Space Telescope Science Institute, which is operated by the Association of Universities for Research in Astronomy, Inc., under NASA contract NAS 5-03127 for JWST. These observations are associated with program #1240.

Some of the data presented in this article were obtained from the Mikulski Archive for Space Telescopes (MAST) at the Space Telescope Science Institute. The specific observations analyzed can be accessed via [10.17909/198x-0r66](https://archive.stsci.edu/10.17909/198x-0r66)

Based on observations obtained at the international Gemini Observatory, a program of NSF NOIRLab,

which is managed by the Association of Universities for Research in Astronomy (AURA) under a cooperative agreement with the U.S. National Science Foundation on behalf of the Gemini Observatory partnership: the U.S. National Science Foundation (United States), National Research Council (Canada), Agencia Nacional de Investigación y Desarrollo (Chile), Ministerio de Ciencia, Tecnología e Innovación (Argentina), Ministério da Ciência, Tecnologia, Inovações e Comunicações (Brazil), and Korea Astronomy and Space Science Institute (Republic of Korea). The work of RML is supported by NOIRLab.

K. D. was supported by NASA through the NASA Hubble Fellowship grant #HST-HF2-51477.001 awarded by the Space Telescope Science Institute, which is operated by the Association of Universities for Research in Astronomy, Inc., for NASA, under contract NAS5-26555. M.M. is grateful for support from a Clay Postdoctoral Fellowship at the Smithsonian Astrophysical Observatory.

Facilities: JWST/MIRI, JWST/NIRSpec, Gemini-N/NIRI

APPENDIX

A. CIRCUMSTELLAR DUST MASS CALCULATION FROM DUSTY PARAMETERS

We demonstrate how the circumstellar dust can be estimated from the DUSTY SED models parameters using the SPHERE geometry, which assumes spherical symmetry in density. The optical depth due to the circumstellar dust, τ_V , which is one of the free parameters in the DUSTY models, can be defined as follows:

$$\tau_V = \int_{R_{\text{in}}}^{R_{\text{out}}} \rho(r) \kappa_V^d dr, \quad (\text{A1})$$

where κ_V^d is the dust opacity, defined here as the dust absorption cross section weighted by dust mass¹⁰, and $\rho(r)$ is the dust density as a function of radius, r , from the center of the circumstellar shell. We define the dust density for the spherical circumstellar shell as

$$\rho(r) = \rho_0 \left(\frac{r}{R_{\text{in}}} \right)^{-\alpha}, \quad (\text{A2})$$

where ρ_0 is the dust density at the inner radius of the dust shell, R_{in} , and α is the power-law index of the radial dust density profile. The dust mass, M_d , is expressed simply by the integral of the dust density over the volume of the circumstellar dust shell with inner radius, R_{in} , and outer radius, R_{out} :

$$M_d = 4\pi \int_{R_{\text{in}}}^{R_{\text{out}}} r^2 \rho(r) dr. \quad (\text{A3})$$

By combining Equations A1, A2, and A3, and substituting R_{out} for the shell thickness parameter $Y = R_{\text{out}}/R_{\text{in}}$, which is an input parameter from DUSTY, the dust mass can be expressed as:

¹⁰ Note that dust opacity may also be defined as the dust absorption cross section weighted by dust *and gas* mass (e.g. De et al. 2023)

$$\begin{aligned}
M_d &= \frac{4\pi\tau_V}{\kappa_V^d} \frac{\int_{R_{\text{in}}}^{R_{\text{out}}} r^{2-\alpha} dr}{\int_{R_{\text{in}}}^{R_{\text{out}}} r^{-\alpha} dr} \\
&= \frac{4\pi\tau_V R_{\text{in}}^2}{\kappa_V^d} \frac{(\alpha-1)(Y^\alpha - Y^3)}{(\alpha-3)(Y^\alpha - Y)}.
\end{aligned} \tag{A4}$$

Assuming a radial density power-law index of $\alpha = 2$, the dust mass of the circumstellar shell is

$$M_d = \frac{4\pi\tau_V R_{\text{in}}^2 Y}{\kappa_V^d}, \tag{A5}$$

Note that R_{in} is a parameter output from the DUSTY modeling.

As an example, in Sec. 3.3.1, the ZTF SLRN-2020 dust mass calculated at the +830 d epoch from with the best-fit DUSTY parameters (Tab. 3) is calculated as follows:

$$\frac{M_d}{M_\odot} \approx 2.4 \times 10^{-11} \left(\frac{R_{\text{in}}}{50 R_\odot} \right)^2 \left(\frac{\tau_V}{0.7} \right) \left(\frac{Y}{5} \right) \left(\frac{\kappa_V^d}{1.123 \times 10^4 \text{ cm}^2 \text{ g}^{-1}} \right)^{-1}. \tag{A6}$$

B. EQUILIBRIUM DUST TEMPERATURE FROM A CENTRAL STELLAR HEATING SOURCE

The balance between the input radiation from a central heating source with luminosity L_* and the thermal emission from circumstellar dust at a temperature T_{eq} can be expressed as follows

$$\frac{L_*}{4\pi r^2} \langle Q_{\text{abs}} \rangle_* = 4 \langle Q_{\text{abs}} \rangle_{T_{\text{eq}}} \sigma_{\text{SB}} T_{\text{eq}}^4, \tag{B7}$$

where r is the separation distance between dust and the heating source, σ_{SB} is the Stefan–Boltzmann constant, $\langle Q_{\text{abs}} \rangle_*$ is the spectrum-averaged absorption cross section from the heating source, and $\langle Q_{\text{abs}} \rangle_{T_{\text{eq}}}$ is the Planck-averaged emission efficiency from the emitting dust (See [Draine 2011](#)).

Assuming the radiation from the heating source can be characterized by a blackbody function at temperature T_* , the spectrum-averaged absorption cross section is defined as

$$\langle Q_{\text{abs}} \rangle_* = \frac{\int B_\nu(T_*) Q_{\text{abs}}(\nu) d\nu}{\int B_\nu(T_*) d\nu}, \tag{B8}$$

where $Q_{\text{abs}}(\nu)$ is the dust absorption efficiency. The Planck-averaged emission efficiency is defined as

$$\langle Q_{\text{abs}} \rangle_{T_{\text{eq}}} = \frac{\int B_\nu(T_{\text{eq}}) Q_{\text{abs}}(\nu) d\nu}{\int B_\nu(T_{\text{eq}}) d\nu}. \tag{B9}$$

The dust absorption efficiency $Q_{\text{abs}}(\nu)$ is commonly approximated as a power-law in frequency/wavelength with index β ($Q_{\text{abs}}(\nu) \propto \nu^\beta$), which is typically assumed to be $0 < \beta < 2$. By adopting the power-law approximation for $Q_{\text{abs}}(\nu)$, it follows that $\langle Q_{\text{abs}} \rangle_{T_{\text{eq}}} \propto T_{\text{eq}}^\beta$.

Assuming that the dust grain size distribution and composition is fixed, the relation between the dust equilibrium temperature and the heating source parameters can be expressed as

$$T_{\text{eq}} \propto \langle Q_{\text{abs}} \rangle_*^{1/(4+\beta)} L_*^{1/(4+\beta)} r^{-2/(4+\beta)}. \tag{B10}$$

C. CONSTRAINTS ON PREVIOUS +320 D SED MODEL PARAMETERS

We conducted a similar analysis using the +320 d circumstellar dust parameters derived by [De et al. \(2023\)](#): $\tau_V = 13$, $T_d = 415$ K, $T_* = 4300$ K, and $R_{\text{in}} = 1143 R_\odot$. The projected circumstellar dust component at +830 d based on the [De et al. \(2023\)](#) parameters would exhibit a $10 \mu\text{m}$ flux of brightness of $\sim 10^{-3}$ Jy, an order of magnitude greater than the $10 \mu\text{m}$ flux measured by the JWST observations at +830 d.

The difference in the $\sim 10 \mu\text{m}$ brightness between the projected dust component from the [De et al. \(2023\)](#) +320 d parameters and ours is due to the differing inner radii ($1143 R_\odot$ vs $4730 R_\odot$), which imply slower moving material for the [De et al. \(2023\)](#) dust component ($\sim 30 \text{ km s}^{-1}$ vs $\sim 120 \text{ km s}^{-1}$). The inner radius and dust temperature from the [De et al. \(2023\)](#) +320 d model are notably consistent with the uncertainties of our +320 d fit (Tab. 3). The projected

+830 d dust temperature from the De et al. (2023) +320 d component is therefore hotter and thus brighter at $\sim 10 \mu\text{m}$ than the projected component from our +320 d model ($T_d^{+830\text{d}} \approx 205 \text{ K}$ vs 100 K). Based on our projected dust emission analysis and the constraints from the JWST observations, we favor the parameters from our +320 d best-fit DUSTY model for the ejecta dust.

REFERENCES

- Agúndez, M., Cernicharo, J., Decin, L., Encrenaz, P., & Teyssier, D. 2014, *ApJL*, 790, L27
- Armstrong, D. J., Lopez, T. A., Adibekyan, V., et al. 2020, *Nature*, 583, 39
- Banerjee, D. P. K., Varricatt, W. P., & Ashok, N. M. 2004, *ApJL*, 615, L53
- Baraffe, I., Chabrier, G., & Barman, T. 2010, *Reports on Progress in Physics*, 73, 016901
- Bear, E., Kashi, A., & Soker, N. 2011, *MNRAS*, 416, 1965
- Bellm, E. C., Kulkarni, S. R., Graham, M. J., et al. 2019, *PASP*, 131, 018002
- Blake, G. A., & Boogert, A. C. A. 2004, *ApJL*, 606, L73
- Böker, T., Beck, T. L., Birkmann, S. M., et al. 2023, *PASP*, 135, 038001
- Bregman, J. D., Lester, D. F., & Rank, D. M. 1975, *ApJL*, 202, L55
- Burgasser, A. J., Bezanson, R., Labbe, I., et al. 2024, *ApJ*, 962, 177
- Calvet, N., & Gullbring, E. 1998, *ApJ*, 509, 802
- Carrera, D., Raymond, S. N., & Davies, M. B. 2019, *A&A*, 629, L7
- Chatterjee, S., Ford, E. B., Matsumura, S., & Rasio, F. A. 2008, *ApJ*, 686, 580
- Dawson, R. I., & Johnson, J. A. 2018, *ARA&A*, 56, 175
- De, K., MacLeod, M., Karambelkar, V., et al. 2023, *Nature*, 617, 55
- De Marco, O., & Izzard, R. G. 2017, *PASA*, 34, e001
- Deleuil, M., Bonomo, A. S., Ferraz-Mello, S., et al. 2012, *A&A*, 538, A145
- Draine, B. T. 2003, *ApJ*, 598, 1017
- . 2011, *Physics of the Interstellar and Intergalactic Medium*
- Drimmel, R., Cabrera-Lavers, A., & López-Corredoira, M. 2003, *A&A*, 409, 205
- Espinoza, N., Rabus, M., Brahm, R., et al. 2017, *MNRAS*, 471, 4374
- Foreman-Mackey, D., Hogg, D. W., Lang, D., & Goodman, J. 2013, *PASP*, 125, 306
- Gordon, I. E., Rothman, L. S., Hargreaves, R. J., et al. 2022, *JQSRT*, 277, 107949
- Gordon, K. D., Clayton, G. C., Decleir, M., et al. 2023, *ApJ*, 950, 86
- Green, G. M., Schlafly, E., Zucker, C., Speagle, J. S., & Finkbeiner, D. 2019, *ApJ*, 887, 93
- Grunblatt, S. K., Saunders, N., Chontos, A., et al. 2023, *AJ*, 165, 44
- Hamer, J. H., & Schlaufman, K. C. 2019, *AJ*, 158, 190
- Hanner, M. 1988, *Grain optical properties.*, In *NASA, Washington, Infrared Observations of Comets Halley and Wilson and Properties of the Grains* p 22-49 (SEE N89-13330 04-89), ,
- Herczeg, G. J., Brown, J. M., van Dishoeck, E. F., & Pontoppidan, K. M. 2011, *A&A*, 533, A112
- Herter, T. L., Henderson, C. P., Wilson, J. C., et al. 2008, in *Society of Photo-Optical Instrumentation Engineers (SPIE) Conference Series*, Vol. 7014, *Ground-based and Airborne Instrumentation for Astronomy II*, ed. I. S. McLean & M. M. Casali, 70140X
- Hodapp, K. W., Jensen, J. B., Irwin, E. M., et al. 2003, *PASP*, 115, 1388
- Holman, M., Touma, J., & Tremaine, S. 1997, *Nature*, 386, 254
- Ivanova, N., Justham, S., Avendano Nandez, J. L., & Lombardi, J. C. 2013, *Science*, 339, 433
- Jackson, B., Barnes, R., & Greenberg, R. 2009, *ApJ*, 698, 1357
- Jellison, E. G., Banzatti, A., Johnson, M. B., & Bruderer, S. 2024, *AJ*, 168, 99
- Kamiński, T., Steffen, W., Tylanda, R., et al. 2018, *A&A*, 617, A129
- Karambelkar, V. R., Kasliwal, M. M., Blagorodnova, N., et al. 2023, *ApJ*, 948, 137
- Kashi, A., Michaelis, A. M., & Feigin, L. 2019, *Galaxies*, 8, 2
- Kashi, A., & Soker, N. 2017, *MNRAS*, 468, 4938
- Keller, L. D., Sloan, G. C., Forrest, W. J., et al. 2008, *ApJ*, 684, 411
- Komarova, O., & Fischer, W. J. 2020, *Research Notes of the American Astronomical Society*, 4, 6
- Labrie, K., Anderson, K., Cárdenes, R., Simpson, C., & Turner, J. E. H. 2019, in *Astronomical Society of the Pacific Conference Series*, Vol. 523, *Astronomical Data Analysis Software and Systems XXVII*, ed. P. J. Teuben, M. W. Pound, B. A. Thomas, & E. M. Warner, 321

- Larson, H. P., Treffers, R. R., & Fink, U. 1977, *ApJ*, 211, 972
- Lau, M. Y. M., Cantiello, M., Jermyn, A. S., et al. 2022, arXiv e-prints, arXiv:2210.15848
- Laughlin, G., & Adams, F. C. 1997, *ApJL*, 491, L51
- Lawrence, A., Warren, S. J., Almaini, O., et al. 2007, *MNRAS*, 379, 1599
- Liu, F., Ting, Y.-S., Yong, D., et al. 2024, *Nature*, 627, 501
- Maciejewski, G., Dimitrov, D., Fernández, M., et al. 2016, *A&A*, 588, L6
- MacLeod, M., Cantiello, M., & Soares-Furtado, M. 2018a, *ApJL*, 853, L1
- MacLeod, M., De, K., & Loeb, A. 2022, *ApJ*, 937, 96
- MacLeod, M., Ostriker, E. C., & Stone, J. M. 2018b, *ApJ*, 868, 136
- Mainzer, A., Bauer, J., Cutri, R. M., et al. 2014, *ApJ*, 792, 30
- Marshall, D. J., Robin, A. C., Reylé, C., Schultheis, M., & Picaud, S. 2006, *A&A*, 453, 635
- Mathis, J. S., Rumpl, W., & Nordsieck, K. H. 1977, *ApJ*, 217, 425
- Matsumoto, T., & Metzger, B. D. 2022, *ApJ*, 938, 5
- Metzger, B. D., Giannios, D., & Spiegel, D. S. 2012, *MNRAS*, 425, 2778
- Munari, U., Henden, A., Kiyota, S., et al. 2002, *A&A*, 389, L51
- Nabbie, E., Huang, C. X., Burt, J. A., et al. 2024, *AJ*, 168, 132
- Naoz, S., Farr, W. M., & Rasio, F. A. 2012, *ApJL*, 754, L36
- Naponiello, L., Mancini, L., Sozzetti, A., et al. 2023, *Nature*, 622, 255
- Nenkova, M., Ivezić, Ž., & Elitzur, M. 2000, in *Astronomical Society of the Pacific Conference Series*, Vol. 196, *Thermal Emission Spectroscopy and Analysis of Dust, Disks, and Regoliths*, ed. M. L. Sitko, A. L. Sprague, & D. K. Lynch, 77–82
- Ossenkopf, V., Henning, T., & Mathis, J. S. 1992, *A&A*, 261, 567
- Patra, K. C., Winn, J. N., Holman, M. J., et al. 2020, *AJ*, 159, 150
- Pinsonneault, M. H., DePoy, D. L., & Coffee, M. 2001, *ApJL*, 556, L59
- Pontoppidan, K. M., Fraser, H. J., Dartois, E., et al. 2003, *A&A*, 408, 981
- Quataert, E., Fernández, R., Kasen, D., Klion, H., & Paxton, B. 2016, *MNRAS*, 458, 1214
- Rasio, F. A., & Ford, E. B. 1996, *Science*, 274, 954
- Rouan, D., Parviainen, H., Moutou, C., et al. 2012, *A&A*, 537, A54
- Salyk, C. 2022, csalyk/spectools.ir: First release, vv1.0.0, Zenodo, doi:10.5281/zenodo.5818682
- Salyk, C., Blake, G. A., Boogert, A. C. A., & Brown, J. M. 2011, *ApJ*, 743, 112
- Salyk, C., Herczeg, G. J., Brown, J. M., et al. 2013, *ApJ*, 769, 21
- Soares-Furtado, M., Cantiello, M., MacLeod, M., & Ness, M. K. 2021, *AJ*, 162, 273
- Soker, N. 2023, *MNRAS*, 524, L94
- Sousa-Silva, C., Seager, S., Ranjan, S., et al. 2020, *Astrobiology*, 20, 235
- Spina, L., Sharma, P., Meléndez, J., et al. 2021, *Nature Astronomy*, 5, 1163
- Stephan, A. P., Naoz, S., & Gaudi, B. S. 2018, *AJ*, 156, 128
- Stephan, A. P., Naoz, S., Gaudi, B. S., & Salas, J. M. 2020, *ApJ*, 889, 45
- Szabó, G. M., & Kiss, L. L. 2011, *ApJL*, 727, L44
- Tylenda, R., Crause, L. A., Górny, S. K., & Schmidt, M. R. 2005, *A&A*, 439, 651
- Tylenda, R., & Kamiński, T. 2016, *A&A*, 592, A134
- Tylenda, R., Hajduk, M., Kamiński, T., et al. 2011, *A&A*, 528, A114
- Vissapragada, S., Chontos, A., Greklek-McKeon, M., et al. 2022, *ApJL*, 941, L31
- Weinberg, N. N., Davachi, N., Essick, R., et al. 2024, *ApJ*, 960, 50
- Weingartner, J. C., & Draine, B. T. 2001, *ApJ*, 548, 296
- Wilson, J. C., Henderson, C. P., Herter, T. L., et al. 2004, in *Society of Photo-Optical Instrumentation Engineers (SPIE) Conference Series*, Vol. 5492, *Ground-based Instrumentation for Astronomy*, ed. A. F. M. Moorwood & M. Iye, 1295–1305
- Wolf, V., Stecklum, B., Caratti o Garatti, A., et al. 2024, *A&A*, 688, A8
- Woodward, C. E., Evans, A., Banerjee, D. P. K., et al. 2021, *AJ*, 162, 183
- Wright, G. S., Rieke, G. H., Glasse, A., et al. 2023, *PASP*, 135, 048003
- Xu, S., Zuckerman, B., Dufour, P., et al. 2017, *ApJL*, 836, L7
- Yarza, R., Razo-López, N. B., Murguía-Berthier, A., et al. 2023, *ApJ*, 954, 176
- Yee, S. W., Winn, J. N., Knutson, H. A., et al. 2020, *ApJL*, 888, L5
- Zahn, J. P. 1977, *A&A*, 57, 383